KU LEUVEN

FACULTY OF SCIENCE

Simulating observables via 3D modelling of disk morphologies in the outflows of evolved stars

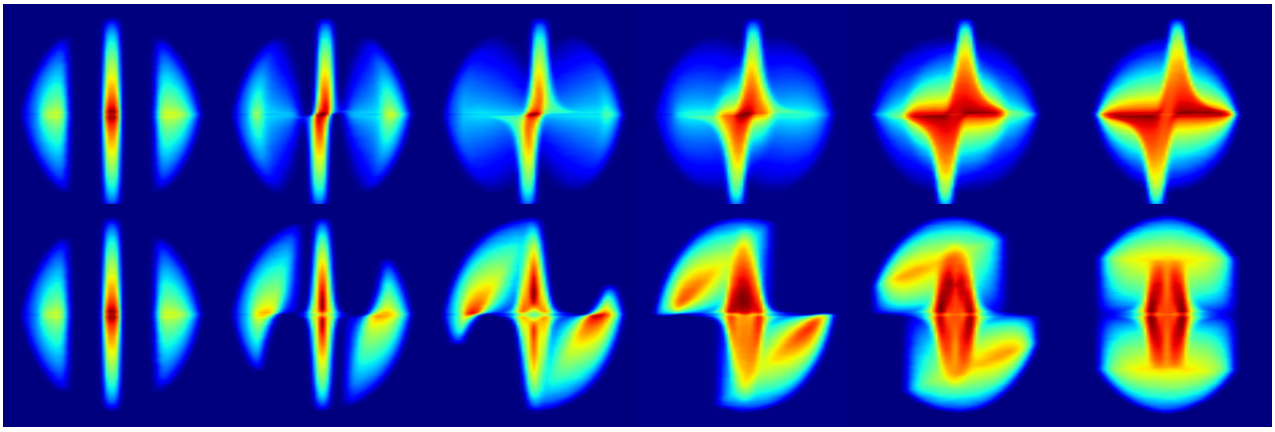

Jels BOULANGIER

Supervisor: Prof. L. Decin

Thesis presented in
fulfillment of the requirements
for the degree of Master of Science
in Astronomy and Astrophysics

Academic year 2014-2015

"Gather ye rosebuds while ye may."

Preface

Evolved low to intermediate mass stars experience tremendous mass loss as they ascend the asymptotic giant branch. The rate at which they expel their outer layers can extend up to $10^{-4} M_{\odot}$ yr^{-1}. Until recently, this mass loss was believed to occur spherically symmetric. Due to continuous improvements in instrumental capabilities, numerous asymmetric structures have revealed themselves in the outflows of these stars. Inferring from two dimensional images which three dimensional complexities are established within these stellar winds, is all but trivial. The aim of this thesis is to provide an overview of observables intrinsic to a disk-like structure combined with a bipolar outflow. Our intention is to lay an intuitive foundation with which upcoming interferometric *ALMA, SMA* and *PdBI* data can be compared and interpreted.

I would like thank my promoter Ward Homan for assisting me in this research. Numerous discussions to interpret the tricky position-velocity diagrams were no luxury. His experience in this research domain really improved the thoroughness of this work. I would also like to thank my supervisor Leen Decin for aiding in the general framework of this thesis. Being able to investigate and contribute to the frontier of complex stellar winds, gave me a feeling of excitement. During my five years in Leuven I have spent an awful lot of time in the student organisation *Wina*. Yet, I am grateful to have experienced this, as it has sculptured the person I am today. Finally, I would like to thank my roommates Boeckx, Goris and De Roover for the endless discussions, support and joyful times.

Summary

As low to intermediate mass stars reach the end of their lives, they ascend the asymptotic giant branch (AGB) where they evolve into large, luminous and cool giants. In this AGB-phase, the stars lose a significant fraction of their mass through stellar winds. The rate at which these stars expel their outer envelopes ranges from 10^{-8} $M_\odot$ yr^{-1} to an astounding 10^{-4} $M_\odot$ yr^{-1}. Thus far, it has been assumed that these stellar outflows are spherically symmetric. However, recent observations with high spatial resolution telescopes have discovered a number of highly complex structures in these outflows. One such morphology is a circumstellar disk with bipolar outflow, generally believed to be formed by binary interactions. The main goal is to be able to infer the three dimensional structure and kinematics from these observations. We aspire to achieve this goal by solving the inverse problem of deriving a three dimensional structure from two dimensional images. The fact that we are only able to observe velocity components projected into our line-of-sight and we have no idea how our object is oriented, makes this even more challenging. Therefore our aim is to provide an overview of observable features intrinsic to that particular morphological structure within the outflows of evolved stars, with the intention of laying an intuitive foundation with which upcoming interferometric *ALMA, SMA* and *PdBI* data can be compared and interpreted. We will achieve this goal by means of an extensive parameter study for which we model rotational CO emission of a simplified analytically parametrised 3D circumstellar disk with a bipolar wind. This description will be fed into a 3D non-LTE radiative transfer code `LIME` which produces 3D intensity maps throughout velocity space. Subsequently, we will manipulate this output into wide-slit position-velocity maps which enables us to compare and analyse the 3D intensity maps. Our modelling will be limited to the $v = 0$ $J = 3 - 2$ CO rotational transition. Additionally, we will investigate the spectral signature of this rotation line.

The PV-diagrams and line profiles are complementary tools to disentangle disk from wind intensity contribution. They allow for the determination of the ratio of mass loss rate and disk mass. Via the introduction of a transition zone between disk and wind, we can make an estimate of the velocity in this region for real astronomical objects. The most apparent effects on the yielded data is, not unexpected, the inclination of the object.

Yet, not all disk and wind properties are deducible from PV-plots or line profiles. We empirically determined that simple analytic temperature and density profiles are indistinguishable. A simple accelerating wind does not yield significantly different output from a constant wind velocity. It is also not possible to derive the amount of flaring at the edges of the circumstellar disk.
Nevertheless, we conclude that spectral signatures and PV-diagrams provide the means to compare and interpret high spectral resolution interferometric data. This thesis provides the building blocks for an extensive archive of simulated observables for disk-like structures in evolved stars which will enable us to gain insight in these intricate objects.

Vulgariserende samenvatting

Sterren met een lage tot gemiddelde massa, tussen de één en acht keer de massa van de zon, evolueren tot grote, koude, heldere sterren wanneer de brandstof voor nucleaire energie productie opraakt. De ster bevindt zich in een fase waar ze heel wat van haar massa verliest door middel van stellaire winden. Tot op heden dacht men dat dit massaverlies mooi sferische symmetrisch was. Maar recentelijk, omwille van de steeds verbeterende instrumenten op onze telescopen, heeft men erg complexe structuren in deze winden waargenomen. Deze gaan van spiralen en schillen tot schijven en donut vormen tot geklonterde structuren. Maar om te kunnen afleiden wat voor vormen er in zo'n sterrenwind schuilt moeten we het probleem omgekeerd aanpakken. Net als medische tomografie en seismolgie, proberen we van een twee dimensionale foto, een drie dimensionaal beeld te creëren. Onze interferometrie telescopen, zoals *ALMA*, meten met welke snelheden delen van de structuren naar ons, of van ons weg, bewegen. Jammer genoeg kunnen we enkel de snelheidscomponent in onze richting, en niet de eigenlijke snelheid, waarnemen. Bovendien kunnen we op geen enkele manier weten hoe de ster, ten opzichte van ons, geörienteerd is. Omwille van deze moeilijkheden stellen wij voor om een overzicht van waarneembare kenmerken te maken. We maken als het ware een fotoalbum dat waarnemers kunnen gebruiken om toekomstige gegevens, van de interferometrie telescopen, mee te vergelijken. In deze thesis beperken wij ons tot een schijfvormige structuur met extra materiaal dat aan de polen wordt uitgestoten.

Contents

CHAPTER 1

Introduction

Low to intermediate mass stars experience a short episode before they undergo a dramatic and fatal transition. Soon the star will stop releasing nuclear energy, become a planetary nebula for a brief moment whereupon it will fade away as a white dwarf. Just before this dramatic change, it will have reached the highest luminosity and largest diameter in its existence. While the star is visible in galaxies far beyond the Local Group, its structure eludes us to this present day. Such a star is called an "asymptotic giant branch star" or "AGB star".

In the early evolution, the so called "E-AGB"-phase, the star is only a bit bluer than its progenitor the red giant branch star (RGB) but besides the core, its structure is similar. It is its second phase that differs fundamentally from RGB stars. In this "thermally pulsation phase", or "TP-AGB", its luminosity exceeds that of any RGB star. This pulsation period is of the order of a one year and will create density enhancements which will allow dust formation. Pulsational engery together with gas-dust interactions will then cause the star to eject material at a high rate, resulting in the end of its nuclear burning phase.
There are several reasons why TP-AGB stars have become quite well studied objects. Firstly the extensive infrared observations with continuously increasing quality. Secondly the availability of highly powerful computers allowing to simulate these very complex objects. Because AGB stars are best detected in the infrared, as they are engulfed within a dust envelope, scientific progress has highly benefited from space observatories such as IRAS, HSO, ISO, MSX and the infrared camera on HST. The *IJHK*-photometry of

large sky survey databases, from the ground, like DENIS and 2MASS, have provided information which turned out to be essential. Radio observations in the (sub)-millimetre regime have given vital information and recent optical surveys such as EROS, MACHO an OGLE unveil new insights in the properties of AGB stars.

The study of AGB stars is of great importance as most stars in the Universe go through this phase of high mass loss. They play a crucial role in the production and ejection of new elements, like s-process nuclei, and dust particles. AGB stars are the main contributors to the enrichment of heavy elements in interstellar medium (ISM), and more generally to the chemical evolution of the Universe. These stars are useful to other fields in astronomy as well because as evolved stars, they provide us with information about the stellar evolution in galaxies.

1.1 Structure of AGB-stars

An AGB star can be decomposed into four different part: (*i*) the small, dense and extremely hot stellar core, (*ii*) the large, still hot but less dense stellar envelope, (*iii*) the sparse and warm atmosphere, (*iv*) and the very large, highly dilute and cool circumstellar envelope. Hence an AGB star covers more than ten orders of magnitude in scale, 30 orders of magnitude in density and seven orders of magnitude in temperature. To fully understand its evolution, we must study the intricate interplay between various physical and chemical interactions. An schematic overview of an AGB star is depicted in Figure 1.1.
The outer atmosphere is cool enough that formation of molecules can take place. Pulsations deposit mechanical energy in the weakly bound outer layers. Thus, the atmosphere becomes largely extended compared to a hydrostatical one. This will give rise to shock formation and at high, therefore cool, enough regions dust can start to condense. These grains are highly sensitive to the stellar UV and optical radiation and get propelled outwards by transfer of radiative momentum. Due to dust-gas collisions, this momentum gets transferred to the gas as well and the dust drags it along into space (Bowen, 1988).
An AGB star will lose mass by means of a slow dusty wind, of the order of 10 km/s, obscuring the central star. At some point, this dusty envelope merges with the surrounding ISM. Here it will take a temperature value of about 10 K while the particle density has dropped to a meagre 10 cm^{-3}. This defines the outer edge of the AGB star and will occur at 10^{16} m or more.

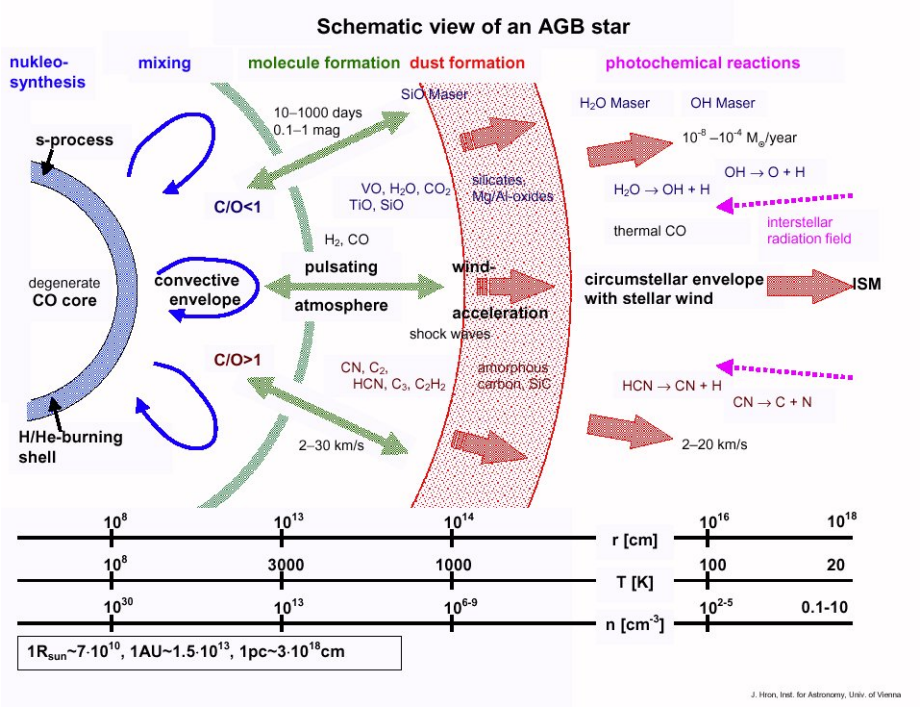

Figure 1.1: An overview of an AGB star (not drawn to scale). Division into four major parts and some important physical/chemical processes are indicated (by J. Hron).

1.2 Pre-AGB evolution

As AGB stars have a mass within the range of $1M_{\odot}$ and $8M_{\odot}$ let us first consider how a low mass AGB star comes into existence. The evolution of such a star in the Hertzsprung-Russell (HR) diagram is illustrated in Figure 1.2. Starting on the zero-age mains sequence, core H-burning occurs radiatively. Due to conversion of H into He the molecular weight changes whereby the central temperature and density rise. This continues until the core is exhausted of H. Gradually the He-core becomes electron degenerate and H-burning is established in a shell surrounding the core. Simultaneously, the star expands and the outer layers become convective. At a certain moment, the convective layer is extended so deeply that it penetrates the layer where partial H-burning occurred in an earlier evolutionary stage. The convective layer can then transport material, from this ^{4}He and CNO products enriched layer, upto the surface. This phenomenon is known as the "first dredge-up". Hereby, surface abundances get altered e.g. the $^{12}C/^{13}C$ ratio changes from about 90 to around 20 and a decrease in $^{12}C/^{14}N$ ratio by a factor of 2.5 (Charbonnel, 1994).

As the star ascends the giant branch in the HR diagram the He core continues to contract and heat up. At the point of maximum temperature the triple-alpha reactions are ignited, resulting in a violent release of energy which is referred to as the "helium-core flash". Immediately after this ignition, the star quickly descends to the horizontal branch where it will quiescently burn He in a convective core and H in a shell around it. In the course of time, the core will be depleted of He and the star begins to ascend the giant branch again. This denotes the star of the E-AGB phase. The core becomes electron degenerate and will start He- and H-shell burning.

More massive stars mainly follow the same track on the HD diagram. However, the He-core burning at the end of the first giant branch now occurs in non-degenerate conditions, resulting in a peaceful He-burning phase when moving to the horizontal branch. Hence no fierce He-core flash. When reaching He-exhaustion of the core, the He-shell burning will result in a strong expansion. As the star ascends the AGB, H-shell burning will halt and the inner edge of the convection outer layer will penetrate this inactive layer. This causes transport of complete H-burning products like ^{4}He, ^{12}C and ^{14}N to the surface, altering its abundances. This is what's called the "second dredge-up". Note that there is critical mass of about $4M_{\odot}$ below which the convective layer cannot penetrate the H-shell, and the second dredge-up does not occur. After this second dredge-up the H-shell is reignited and the star continues to move up the AGB.

1.3 AGB evolution

As helium gets depleted in the core (He-exhaustion in Figure 1.2) the carbon-oxygen core starts to contract up till it has reached the density of a white dwarf. It has now a size of about 10^6 m and a temperature of 10^8 K. This contraction brings with it an increase in luminosity and expansion of the stellar envelope. This latter reaches a size of 10^{11} m with a surface temperature of about 3000 K. The C-O core is supported by degenerate electrons, the requirement sets an upper mass limit of the AGB star at about 8 $M_{\odot}$. When the star has reached a luminosity of approximately the tip of the RGB, 3000 $L_{\odot}$ (Bedding & Zijlstra, 1998), the star is able to both burn H and He in shells. Schwarzschild & Härm (1965) and Weigert (1966) independently found that the He-shell burning on the AGB does not proceed smoothly but is subjected to thermal instabilities. This He-shell burns, on a regular basis, rapidly into carbon. This ensures a moderate luminosity raise, which is referred to as a "He-shell flash" or "thermal pulse". Between consecutive pulses, the H-shell starts to burn again and provides the luminosity of the star. This alternating process is what's called the "TP-AGB phase".
During the thermal pulse the convective layer can reach the parts which are

enriched with nuclear products and bring them to the surface. Mainly fresh carbon from the inner regions gets transported and in some stars this enrichment of the surface can continue long enough for the abundance of carbon to exceed that of oxygen, creating carbon-rich AGB stars[1]. This process is called the "third dredge-up". Note that even though low mass AGB stars have not experienced a second dredge-up, this is always referred to as the third dredge-up.
The pulsational behaviour of the star, together with dust-gas interactions will expel the weakly bound outer regions of the star. Ultimately, the rate of this ejection will exceed the growth rate of the core. From this point onward, the mass loss determines the evolution of the star. Eventually, all material around the core has been blown away, this sets the endpoint of the AGB era and the beginning the post-AGB epoch. This latter only last for a short period of time, of the order of a thousand years, before it turns into a planetary nebula. The core fades out as a white dwarf, yet still ionising and therefore illuminating the expanding nebula, giving rise to one of the most spectacular and colourful astronomical phenomena.

Due to their short life time, maximally upto 2% of the time it spends on the main sequence (Vassiliadis & Wood, 1993), AGB stars will not widely populate the Universe. Olivier et al. (2001) estimate the local column density of dust-enveloped AGB stars to be $(15\pm4)\cdot10^{-6}$ stars per pc^2. Comparing with a local column density of 30 main sequence stars and 3 white dwarfs (Cox, 2000), we can conclude that AGB stars are rare!

[1]As the C/O ratio in the interstellar medium is below unity, all AGB star are born oxygen-rich.

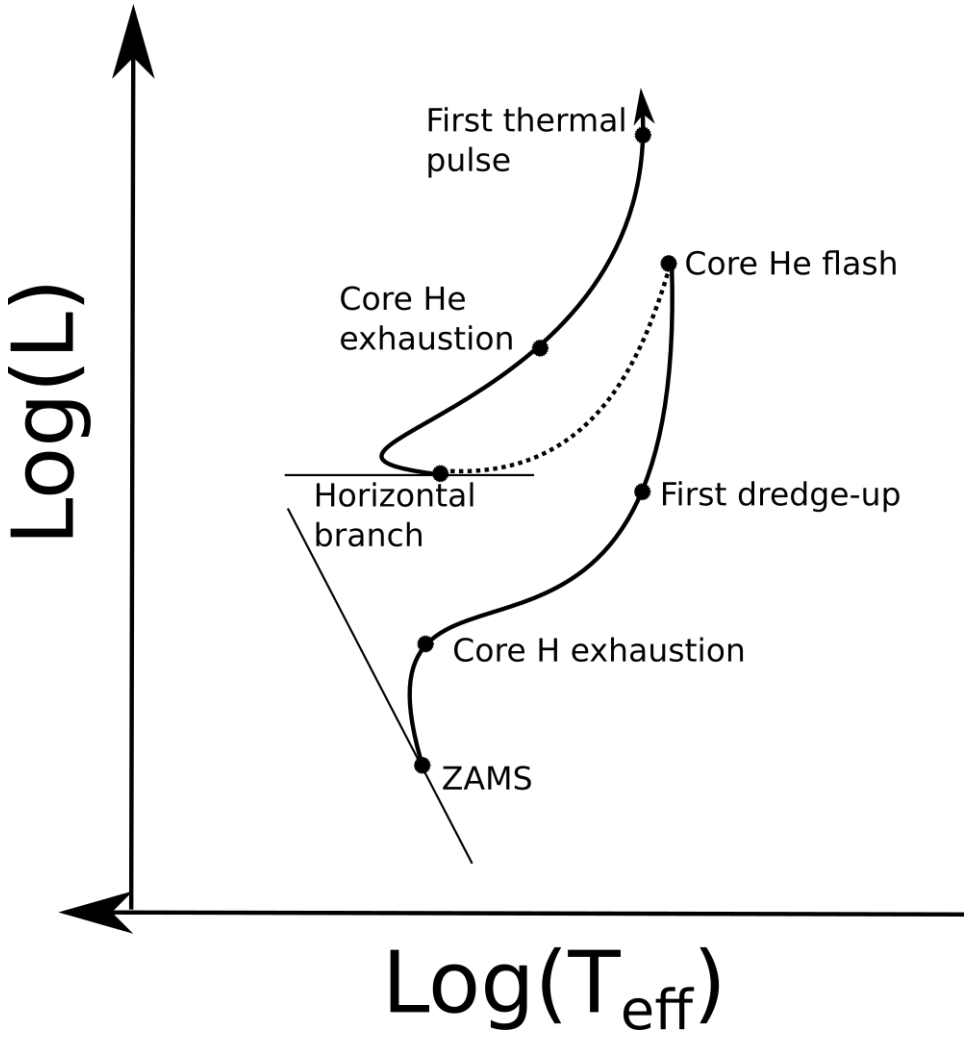

Figure 1.2: Schematic evolution of a star of $M \approx 1 M_{\odot}$.

1.4 Overview

In this AGB-phase, the stars lose a significant fraction of their mass through stellar winds. The rate at which these stars expel their outer envelopes ranges from 10^{-8} $M_{\odot}$ yr^{-1} to an astounding 10^{-4} $M_{\odot}$ yr^{-1} (De Beck et al., 2010). These winds are driven due to a combination of radiative pressure on dust grains and a pulsation behavior of the star (Bowen, 1988). Thus far, it has been assumed that these stellar outflows are spherical symmetric. Recent observations with high spatial resolution telescopes, however, have discovered a number of highly complex structures in these outflows. This includes bipolar structures (e.g. Balick et al., 2013), disks (e.g. Jeffers et al., 2014; Lykou et al., 2015; Chiu et al., 2006; Hirano et al., 2004), arcs (e.g. Decin et al., 2012; Cox

et al., 2012), shells (e.g. Mauron & Huggins, 2000), spirals (e.g. Maercker et al., 2012; Kim et al., 2013; Maercker et al., 2014), clumps (e.g. Bowers & Johnston, 1990), tori (e.g. Skinner et al., 1998) and bubbles (e.g. Ramstedt et al., 2014). Several mechanisms may be responsible for the formation of these structures. Shells and arcs may be caused by temporal variations in the mass loss rate and/or expansion velocity (Maercker et al., 2014, and references therein). Aspherical structures may be the result of non-isotropic mass loss (e.g. Ueta, 2006), systemic motion with respect to the ISM (e.g. Decin et al., 2012), magnetic fields (e.g. Pérez-Sánchez et al., 2013; van Marle et al., 2014) or binarity (Soker, 1997; Huggins, 2007; van Winckel et al., 2009).

Due to recent improvements of observational techniques and instruments, we are capable to probe the inner regions of dust envelopes surrounding stellar objects. The high spatial resolution that interferometry can provide, enables us to distinguish complex structures on a scale like never before. Especially, the most recent asset in interferometric capabilities, the Atacama Large Millimeter/submillimeter Array (*ALMA*) is an extremely powerful tool to acquire knowledge about the complex structures within these dusty envelopes. It is ideal for observing regions close to a star, proto-planetary disks, black hole accretion disks and, thus far obscured, complexes within stellar winds of evolved stars. This latter is of most interest for this thesis as our aim is to provide an overview of observable features intrinsic to certain morphologies of the structure within this outflow. Similar research has been done for a spiral structure (Homan et al., 2015)
The interferometric output that *ALMA* yields is not self-evident to interpret. Its output is a 3D data cube with two spacial axes and one velocity axis. *ALMA* measures the amount of emission of a certain transition line of a certain molecule in the line-of-sight. Due to the Doppler shift, with respect to the central wavelength of the line, the velocity of that emitting region is known. Hereby, you know which regions of the structure move away or towards you and with what velocity. A first issue is that the objects we observe are three dimensional and we are only able to obtain a 2D spatial image. A next problem arises as the measured velocity of different regions is not their actual velocity but the projected one in the line-of-sight. Furthermore, the orientation of the object is not known. These issues make it very challenging to deduce the true morphology of the objects just from the 3D data cube. The way to tackle this problem is by inverting the process. Start with analytic created structures based on our theoretical understanding, generate simulated *ALMA* data for these objects and compare observed data with an archive of simulated data. Based on the results, the model is improved to give a better fit.

In this thesis, we focus on a *Keplerian* disk structure with a bipolar out-

flow. The disk acts as a collimator of mass loss subsequently creating a bipolar outflow. Our object is a compilation of different observationally determined structures in AGBs, post-AGBs and PNs. Kervella et al. (2014) determined that a dusty disk surrounds the AGB star L_2 Pup. Jeffers et al. (2014) discovered that there is a axisymmetrically expanding disk present around the carbon-rich AGB star CW Leo. A rotating disk with a slow expansion velocity was found by Lykou et al. (2015). This would make it the firstly discovered Keplerian rotating AGB-disk. But also more complex velocity fields have been found in AGB disks. Chiu et al. (2006) and Hirano et al. (2004) determined that their objects, π^1 Gru and V Hya respectively, have an expanding disk with a fast bipolar outflow. The former star seems to have a slow equatorial wind as well, while the latter possesses an intermediate outflow between disk and bipolar outflow.
Contrary to our suggested object, disks around post-AGB stars and young planetary nebula are not observed to rotate but to expand symmetrically (like the rest of the nebula) (Alcolea et al., 2007; Castro-Carrizo et al., 2012). These expanding structures are often thought to be the remnants of former AGB winds. Yet recently, three remarkable exception have been found: the Red Rectangle, AC Herculis and HR 4049. Bujarrabal et al. (2005) found the inner disk of the Red Rectangle to be rotating *Keplerian*. In addition, a very slow (< 1 km/s) expansion is present. Bujarrabal et al. (2015) have clearly detected *Keplerian* dynamics in a disk orbiting AC Her. This object, however, does not show evidence of expansion. The post-AGB star HR 4049 comprises a Keplerian disk in addition with an expansion component (Malek & Cami, 2014). Additionally, Bujarrabal et al. (2013) observed four post-AGB objects which possess indications of surrounding rotating disks. One of them, the Red Rectangle we already discussed. Observations of post-AGB stars and planetary nebula, for which AGB stars are the progenitors, provide evidence for the bipolar structure (Bujarrabal et al., 2013, 2015; Kraemer et al., 2010; Balick & Frank, 2002, and references therein).
As stated by van Winckel et al. (2009), the presence of a dusty *Keplerian* disk is an indication of a binary nature of the object in post-AGB stars. Binarity of the central object has been confirmed for the post-AGB star AC Her (Bujarrabal et al., 2015). García-Segura et al. (2014) have tested whether a single star can sustain rotational velocities in the circumstellar envelope from magnetohydrodynamical (MHD) simulations aiming at creating bipolar planetary nebula in the case of high mass loss rates. They conclude it is unlikely for single rotating stars to be the progenitors of bipolar planetary nebula (under the current MHD model paradigm).

We will make no assumptions on the disk formation mechanisms. Alternatively, its presence will be assumed and it will be shown how these morphological structures manifest themselves in observable quantities by means

of 3D radiative transfer calculations. As stated before, profiles of physical quantities, like temperature, density and velocity are described analytically and its emission is modelled with `LIME`, a fully three-dimensional non-local thermodynamical equilibrium (non-LTE) radiative transfer code (Brinch & Hogerheijde, 2010). Arguably, a complete analytic description of the physical quantities might not be very coherent with reality. However, it enables us to calculate a vast grid of models, something which at present time is virtually impossible to achieve via radiative-hydrodynamical calulations.
In general, predicting the radiation signature of an object can be done by solving the radiation transport equation. In the special case of non-LTE, a statistical equilibrium of the atomic and molecular quantum states must be uphold. This latter together with the radiative transfer, is a strongly coupled set of equations that need to be solved simultaneously. This can only be done numerically except for the special cases where either the material is in LTE or in the optically thin regime where there is little interaction between matter and radiation. The strain on computational power increases rapidly with increasing complexity of the structure if such approximations are not valid. Due to the low density regimes, often found in inter- and circumstellar environments, LTE is not a valid approximation and therefore the atomic/molecular excitations need to be solved numerically. `LIME` is a cutting-edge radiative transfer code, especially designed for complex 3D frameworks, which solves the coupled system of quantum state populations without approximations and, just like *ALMA*, yields a 3D data cube output.

Comparison of the raw 3D data cubes is not very efficient nor practical. Therefore, a manipulation to position-velocity (PV) maps and line profiles of the entire object are means to more easily interpret and compare results. A PV-diagram is a slice through the 3D data cube in any direction but preserving the velocity axis. A graphical interpretation is given in Figure 1.3. As the width of this slice is only one pixel, it gives us little information about the whole structure. When increasing the width of the slice, all data points in a column along the width are summed up. This width can be extended such that it engulfs the entire cube. This latter is most useful as one gains insight into the global structure, e.g. how much material is moving with a certain velocity. For the purpose of this thesis, a slice preserving velocity- and x-axis and one preserving velocity- and y-axis are most suitable as our object is analytically created and therefore we know how it is oriented. Hence, a slice of full-cube width will consist of all information projected on the x- and y-axis respectively. Due to this analytic approach, it is more easy to ascertain which regions contribute to the total flux and why features are established in a particular manner. The advantage of a PV diagram is that is better shows correlated structure and by to the collapse of material, increases the signal-to-noise.

When integrating the intensity over the whole spatial part of the cube, for each velocity, one creates a line profile. Such a line profile is helpful for large structure determination and comparison. It will be an easy tool to distinguish between different orientations of the object as the orientation is crucial for the projected velocity. The amount of material that is moving, or flux that is emitted at a certain projected velocity is exactly what information the line profile holds. The whole process of manipulating the 3D data cube, is illustrated in Figure 1.4.

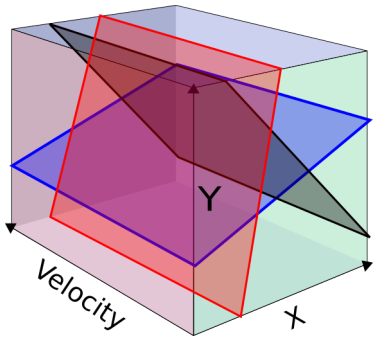

Figure 1.3: A number of possible slices through the 3D data cube by preserving the velocity axis.

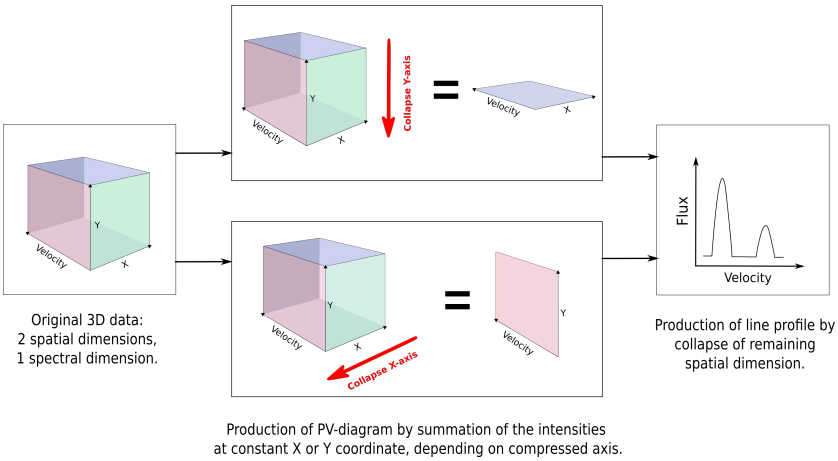

Figure 1.4: The complete description to manipulate the 3D data cube into PV diagrams and spectral line profiles.

CHAPTER 2

Radiative transfer

In a non-LTE environment, thermodynamic and microscopic processes need not to be in balance, but the level populations must not change in time. This means that a statistical equilibrium is reached and the population n_i of an energy level i satisfies:

$$\frac{dn_i}{dt} = \sum_{j \neq i}^{N} n_j P_{ji} - n_i \sum_{j \neq i}^{N} P_{ij} = 0 \tag{2.1}$$

where N is the total number of states that can influence the population of the level of interest. P_{ij} is the probability of a transition from level i to level j, also known as the transition rate. These transition rates can be decomposed in several components: spontaneous radiative emission; stimulated radiative emission; radiative absorption and collision excitation/de-excitation,

$$P_{ij} = A_{ij} + B_{ij}\overline{J_\nu} + C_{ij}. \tag{2.2}$$

where $\overline{J_\nu}$ is the mean radiation field and the meaning of the coefficients will be explained below. The major difficulty for these non-LTE calculations is the vast number of coupled equations, the transition rates P_{ij} depend on the mean radiation field, for which we need to know the specific intensity I_ν in all directions. This latter depends on the source function $S_\nu = j_\nu/\alpha_\nu$ where j_ν and α_ν are the emission and absorption coefficients respectively. These, on their turn depend on the energy level populations, for which we need the transition rates P_{ij}. Therefore, these population equations need to be solved simultaneously with the radiative transfer equation

$$\frac{dI_\nu}{ds} = \frac{j_\nu}{4\pi} - \alpha_\nu I_\nu. \tag{2.3}$$

The specific intensity I_ν is the amount of energy per unit time and frequency which passes through a surface area dA at an angle θ into a cone of solid angle $d\Omega$ at a frequency ν. Here s is distance and j_ν and α_ν are the emission and absorption coefficients respectively. The units of specific intensity are J s^{-1} m^{-2} sr^{-1} Hz^{-1} or Jy sr^{-1}.

2.1 Spontaneous radiative emission

The probability that an electron of level u will decay spontaneously to a lower level l is called the Einstein coefficient of spontaneous emission A_{ul}. This transition probability is inherent to the atomic/molecular structure and therefore independent of the local thermodynamic and/or chemical conditions. The total number of transition R_{ul}, is this Einstein coefficient multiplied by the number density of the level u,

$$R_{ul} = n_u A_{ul}. \tag{2.4}$$

If there are multiple decay possibilities, the different Einstein coefficients just add.

2.2 Radiative absorption

The population of a level can increase by absorption of a photon with the energy equal to that of a difference in level energies. Obviously, this depends on the radiation field which the atom/molecule is subjected to. Since not the direction of the photons but only the amount of them is important, it is the mean intensity

$$J_\nu \equiv \frac{1}{4\pi} \int I_\nu d\Omega \tag{2.5}$$

which is relevant. J_ν has units J s^{-1} m^{-2} Hz^{-1} or Jy. As the energy levels are not infinitely sharp, their broadening is characterized by a line profile function $\phi(\nu - \nu_0)$ which contains different broadening mechanisms. This profile function is normalized to unity when integrated over frequency. The number of photons that can contribute to the transition is weighted by this function such that:

$$\overline{J^\phi_{\nu_0}} \equiv \frac{\int_0^\infty J_\nu \phi(\nu - \nu_0) d\nu}{\int_0^\infty \phi(\nu - \nu_0) d\nu} = \int_0^\infty J_\nu \phi(\nu - \nu_0) d\nu \tag{2.6}$$

where ν_0 is the frequency between the levels u and l. The probability of this type of transition is denoted by the Einstein coefficient B_{lu}. Hence, the total number of transitions from level l to u via radiative absorption is given by

$$R_{lu} = n_l B_{lu} \overline{J^\phi_{\nu_0}}. \tag{2.7}$$

2.3 Stimulated radiative emission

It is also possible to emit a photon by absorbing a photon of the same energy. This processes is called stimulated emission and, obviously, also depends on the radiation field. The transition rate is similar to the radiative absorption but the weighted line function need not to be the same.

$$\overline{J^{\chi}_{\nu_0}} = \int_0^{\infty} J_{\nu}\chi(\nu - \nu_0)d\nu \tag{2.8}$$

Also, a third Einstein coefficient B_{ul} is introduced. The total number of transitions from level u to l is given by

$$S_{ul} = n_u B_{ul} \overline{J^{\chi}_{\nu_0}}. \tag{2.9}$$

The Einstein relations, relate the different Einstein coefficients,

$$\frac{B_{lu}}{B_{ul}} = \frac{g_u}{g_l} \qquad \text{and} \qquad \frac{A_{ul}}{B_{ul}} = \frac{2h\nu^3}{c^2}. \tag{2.10}$$

These are two equations with three unknowns, so only one coefficient has to be constrained in order to know them all.

2.4 Collisional excitation/de-excitation

The collision rate to go from a level u to a level l is equal to

$$C_{ul} = n_{col}\gamma_{ul} \tag{2.11}$$

where n_{col} is the number density of the collision partner and γ_{ul} is the downward collision rate coefficient (in cm^3 s^{-1}). The rate coefficient is the Maxwellian average of the collision cross-section σ,

$$\gamma_{ul} = \left(\frac{8kT}{\pi\mu}\right)^{-1/2} \left(\frac{1}{kT}\right)^2 \int_{E_0}^{\infty} \sigma E e^{-E/kT} dE \tag{2.12}$$

where k is the Boltzmann constant, μ is the reduced mass of the system, E is the center-of-mass collision energy and E_0 is the threshold energy which is needed for the process to take place (Schöier et al., 2005). As the velocities of the particles are Maxwellian, detailed balance is satisfied and can be used to calculate the collision rate coefficient for the upward transition,

$$\gamma_{lu} = \gamma_{ul}\frac{g_u}{g_l} e^{-h\nu/kT}, \tag{2.13}$$

where g is the statistical weight and T the temperature of the gas. The total number of transitions for an upward or downward collisional transition are given by

$$R_{ul} = n_u C_{ul} \qquad \text{and} \qquad R_{lu} = n_l C_{lu} \tag{2.14}$$

respectively.

2.5 Transfer equation and level populations

The spontaneous de-excitation of electrons is isotropic, therefore, the total energy output per second and per Hz radiated per unit volume is:

$$j_\nu^{spont} = h\nu_0 n_u A_{ul} \psi(\nu - \nu_0). \tag{2.15}$$

The total energy lost by radiative excitation per unit volume per unit time is:

$$dE_{tot} = h\nu_0 n_l B_{lu} \overline{J_{\nu_0}} dV dt \tag{2.16}$$

$$= h\nu_0 n_l B_{lu} dV dt \int J_\nu \phi(\nu - \nu_0) d\nu \tag{2.17}$$

$$= h\nu_0 n_l B_{lu} dV dt \int\int \frac{I_\nu}{4\pi} \phi(\nu - \nu_0) d\Omega d\nu. \tag{2.18}$$

When considering only the energy absorbed through a solid angle $d\Omega$, in a frequency range $d\nu$ during dt in a volume dV,

$$dE = \frac{h\nu_0}{4\pi} n_l B_{lu} I_\nu \phi(\nu - \nu_0) d\Omega d\nu dV dt. \tag{2.19}$$

Knowing that $dV = dAds$ and with the definition of the absorption coefficient $dI_\nu = -\alpha_\nu I_\nu ds$, the absorption coefficient of radiative excitation is given by:

$$\alpha_\nu^{rad.exc.} = \frac{h\nu_0}{4\pi} n_l B_{lu} \phi(\nu - \nu_0). \tag{2.20}$$

Emission by stimulated radiation is more convenient as a negative component of the absorption coefficient as it also depends on the radiation field. Hence, the radiative absorption coefficient is:

$$\alpha_\nu = \frac{h\nu_0}{4\pi} \left[n_l B_{lu} \phi(\nu - \nu_0) - n_u B_{ul} \chi(\nu - \nu_0) \right] \tag{2.21}$$

Hence, the radiative transfer equation (2.3) has an emission coefficient j_ν given by equation (2.15) and an absorption coefficient α_ν as in equation equation (2.21). Assuming statistical equilibrium (2.1), the population of the i'the level is given by:

$$n_i = \frac{\sum_{j \neq i} n_j P_{ji}}{\sum_{j \neq i} P_{ij}} \tag{2.22}$$

$$= \frac{\sum_{j>i} n_j \left[A_{ji} + B_{ji} \overline{J_{ji}} + C_{ji} \right] + \sum_{j<i} n_j \left[B_{ji} \overline{J_{ji}} + C_{ji} \right]}{\sum_{j<i} \left[A_{ij} + B_{ij} \overline{J_{ij}} + C_{ij} \right] + \sum_{j>i} \left[B_{ij} \overline{J_{ij}} + C_{ij} \right]} \tag{2.23}$$

$$= \frac{\sum_{j>i} n_j A_{ji} + \sum_{j \neq i} n_j \left[B_{ji} \overline{J_{ji}} + C_{ji} \right]}{\sum_{j<i} A_{ij} + \sum_{j \neq i} \left[B_{ij} \overline{J_{ij}} + C_{ij} \right]} \tag{2.24}$$

where $\overline{J_{ij}}$ denotes the weighted mean intensity over the frequency between the i'th and j'the level, cfr. Eq (2.6) and Eq. (2.8). Because $\overline{J_{ij}}$ is implicitly dependents on n_i and n_j via j_ν and α_ν, equations (2.5) and (2.24) need to be solved iteratively.
This whole problem is further complicated if a velocity field is present. Hereby, photons get Doppler shifted and contribute to other transitions if the energy levels are spaced closely enough. This is not a problem for molecules like CO which has sufficiently widely spaced energy levels, but for more complex molecules this is a serious concern.

CHAPTER 3

3D non-LTE radiative transfer code

In order to predict the emergent spectra of our object of interest, the molecular/atomic excitation and the radiation transfer problem need to be solved. For this, a 3D non-LTE radiative transfer code, named `LIME` (Line Modelling Engine, Brinch & Hogerheijde, 2010), is used. It has specifically been created for the (sub-)millimeter and far-infrared regime and works in arbitrary geometries (3D). This code has been designed to be fast, reliable and easy to use with emphasis on solving models with high spectral resolution, relevant for *ALMA*, and complex level configurations, relevant for Herschel. `LIME` has been written for the purpose of solving disks and envelopes around young stellar objects (YSOs) but due to its 3D nature, it can be used to model more complex structures like outflows, molecular clouds and even clusters of YSOs and their environment. For a technical overview and inner workings of the code, see Brinch & Hogerheijde (2010). The original code was developed to solve radiative transfer in molecular clouds and not to model stellar winds. For this latter, the central mass-losing star is a non-negligible source of energizing photons. For this reason `LIME` has been adapted to have an option to position an arbitrary number of stars at locations of choice.

`LIME` tries to determine the level populations by solving Eqs. (2.5) and (2.24) iteratively. The radiative transfer equation contains the emission and absorption coefficients, j_ν and α_ν respectively which, for the gas, are governed by equations (2.15) and (2.21) as these are line transitions. The continuum

thermal dust emission has

$$j_\nu^{\text{dust}} = -\alpha_\nu^{\text{dust}} B_\nu(T_{\text{dust}}) \tag{3.1}$$

$$\alpha_\nu^{\text{dust}} = \kappa_\nu \rho_{\text{dust}} \tag{3.2}$$

with $B_\nu(T_{\text{dust}})$ a Planck curve for a certain dust temperature and κ_ν and ρ, the opacity and mass density of the dust. The scattering term σ_ν in the transfer equation is neglected because the cross-sectional efficiency strongly decreases with wavelength, $Q^S \propto \lambda^{-4}$ whereas the absorption efficiency goes as $Q^A \propto \lambda^{-p}$ with $p = 1$ for $1 < \lambda < 30$ μm and $p = 2$ for larger wavelengths. Therefore the scattering is of little relevance in the (sub)-millimeter regime. `LIME` considers thermal and Doppler broadenig effects for the line profile functions in Eqs. (2.15) and (2.21) since the latter is the dominating broadening mechanism due to local turbulence. The collision rate coefficients, defined by Eq. (2.12), are read in from an external file provided by the LAMDA database[1]. These are also used to calculated the rate coefficients for upward transitions via Eq. (2.13).
As the CO molecule only has a tiny dipole moment, it will barely interact radiatively. The level populations of CO are therefore mainly determined by collisional interaction which is very temperature dependent, cfr. Eq. (2.12).

3.1 Computational grid

As opposed to the wide use of a Cartesian or cylindrical grid, `LIME` uses a more randomly generated grid. A random point distribution weighted with the density profile(s) of the object is used. This has advantages from a radiative perspective as by this means, the radiation producing (and absorbing) regions are well sampled. Furthermore, as the mean distance between two points will become inversely proportional to the density, it will become proportional to the mean free path l_ν , since $l_\nu = (\alpha_\nu \rho)^{-1}$. For continuum radiation transfer, for which α_ν is independent of the radiation field, the mean free path can be set equal to the average distance between two grid points $\langle d \rangle$ by changing the number of grid points such that $\langle d \rangle \propto \kappa_\nu$. Because if $l_\nu = \langle d \rangle$:

$$\begin{aligned} l_\nu &= (\alpha_\nu \rho_d)^{-1} \\ l_\nu &= (\kappa_\nu \rho_d^2)^{-1} \\ l_\nu &\propto \kappa_\nu^{-1} \langle d \rangle^2 \\ \langle d \rangle &\propto \kappa_\nu \end{aligned}$$

Where in the first step we used Eq. (3.2), for the second step the property of the gridding which makes the distance between two points inversely proportional to the density, $\langle d \rangle \propto \rho^{-1}$, is used. The last equality arises from our

[1] http://home.strw.leidenuniv.nl/ moldata/

begin statement, $l_\nu = \langle d \rangle$.

For line radiation transfer, α_ν is not that straightforward since it depends on the radiation field and the current level populations. Therefore, the mean free path is frequency dependent. Nevertheless, gridding with a density weighted function is the best option as this describes the spatial distribution of the molecules very well. Each of these grid points contains the physical information (temperature, density, velocity, populations, etc.) of the surrounding area.

Once the grid points have been distributed, they are connected by Delaunay triangulation. In 2D, this triangulation is such that for a set of points P, there is no point $s \in P$ that lies within the circumcircle of any triangle created by this triangulation. In 3D, the connected points form tetrahedra with no grid points within their circumsphere. Corresponding to this, Voronoi cells, which are the dual graph of the Delaunay triangulation, are created. Concretely, the centers of the circumspheres are connected and each Voronoi cell contains one grid point. Every point (not grid point) within this cell lies closer to that grid point than to any other grid point. All physical information a grid point contains, applies to the region spanned by its Voronoi cell. A 2D representation of such Delaunay triangulation and Voronoi cells is illustrated in Figure 3.1. Due to the stochastic nature of this sampling method, it is inevitable that some grid points end up much closer or further than the expected local separation value. This causes long, narrow triangles which are unwanted for photon propagation. Therefore, each grid point is moved slightly away from its nearest neighbour over an iterative process. Moving the points too slowly or iterate too much will cause the grid to become Cartesian. Brinch & Hogerheijde (2010) empirically found that using 25 iterations and moving the grid points about 10% away from its neighbours results in a smooth grid which still provides the underlying physical structure. The boundary of the grid contains a user specified number of grid points. These grid points just represent the end of the computational grid and when a photon reaches this sink point, it is considered to have escaped the model.

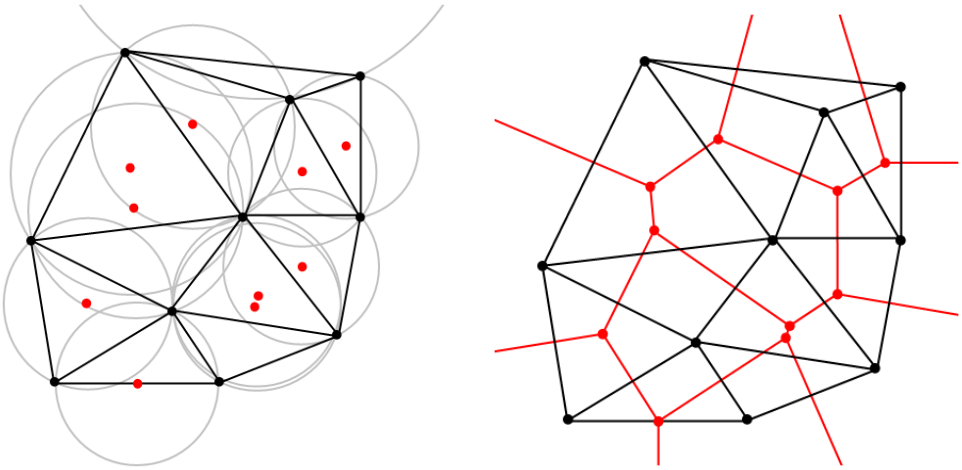

Figure 3.1: *Left:* Delaunay triangulation of grid points (black) with all the circumcircles (grey) and their corresponding origins (red). *Right:* Voronoi cell creation around grid points (black) by connecting the centers of the circumcircles (red).

3.2 Photon propagation

In order to determine to level populations at a certain grid point, one needs to know the mean radiation field $\overline{J_\nu}$ this point receives. To obtain this, a path of incoming photons must be recreated. `LIME` sends out a package of photons[2] from this specific grid point to create the path. The photons get propagated along the Delaunay lines which makes solving Eq.(2.3) easy and fast as the directions from where the radiation field is coming, are limited. Ritzerveld & Icke (2006) have shown that via a Delaunay triangulation, each grid point is connected to approximately sixteen neighbours. The sampling of the radiation field J_ν is thus on average limited to this number. To recreate the incoming path of radiation, a package of photons is send from the specific point to its neighbours. But, to properly sample the frequency spectrum and conserve photon momentum, a lot of photons need to propagate along each Delaunay line. In reality, when a photon gets absorbed, the molecule can re-emitted one isotropically and will move in the corresponding direction to conserve momentum. As our model has fixed grid points, momentum cannot be conserved in this way. But on average, after enough interactions, the photon will move along the direction it got absorbed and the molecule will stay at rest. This solves the problem of fixed grid points but due to the random orientation of the Delaunay lines, the photon cannot continue to

[2] `LIME` actually does not send out photons but a distribution function of the specific intensity I_ν is transmitted between grid points. This specific intensity is calculated according to Eq. (3.5)

move in a straight line. Instead the photon will get propagated via one of the two Delaunay lines which makes the smallest angle with the initial direction (first Delaunay line). The probability to choose either lines is weighted with the ratio of both angles

$$P(l_2) = \frac{\alpha_1}{\alpha_2} P(l_1), \tag{3.3}$$

where $\alpha_1 < \alpha_2$. This propagation continues for all subsequent grid points until the photon escapes the model. This procedure is carried out for a number of initial photons creating not a line-of-sight but rather a light cone, as illustrated in Figure 3.2, which averages out the photon directions which are not along the line of the initial one, hence conserving momentum. Such a cone is constructed along each initial Delaunay line of the grid point. `LIME` then verifies if by this means, the whole grid is sampled. If not, more photons are send through the initial Delaunay lines creating larger cones as the probability for other lines is small but not zero. Note that all photons are sampled properly over a frequency range to account for all possible transitions.
Each grid point will see more photons coming from high density regions as these have more Delaunay connections due to the grid sampling method. Because of this, one should be careful when averaging the radiation field. Equation (2.5) becomes a direct sum

$$J_\nu = \frac{1}{4\pi} \sum_i^N I_{i,\nu} \Omega_i \tag{3.4}$$

where N is the number of Delaunay neighbours and Ω_i is the corresponding solid angle. Strictly speaking, a solid angle is the surface area on a sphere but here, we will use the surface area of the Voronoi cell of that Delaunay line, which within 10%, is a good approximation.
The radiation field is obtained by integrating Eq. (2.3) over all contribution grid points. The area between a grid point and the edge of its Voronoi cell is assumed to be a homogeneous slab, hence the solution is of the form:

$$I_\nu(\tau_\nu) = I_\nu(0) e^{-\tau_\nu} + S_\nu(1 - e^{-\tau_\nu}), \tag{3.5}$$

where S_ν is the source function and $\tau_\nu = \alpha_\nu ds$ is the optical thickness between the grid point and the edge of its cell, a distance ds from each other. The total specific intensity I_ν is then used in equation (3.4) to acquire the total radiation field J_ν. The radiation field is integrated upto the edge of the grid at which point also any external contribution is added, which in most cases is the cosmological background radiation.
When trying to determine the level populations, one of the key aspects is of course determining if an equilibrium has been reached. Brinch & Hogerheijde (2010) determined that it is impossible to have a simple criterion in the code which checks if the model has converged. They empirically established that

15-20 iterations is enough to ensure equilibrium. Keep in mind that this is highly dependent on the polarity and complexity of the molecule as well as the density scale.

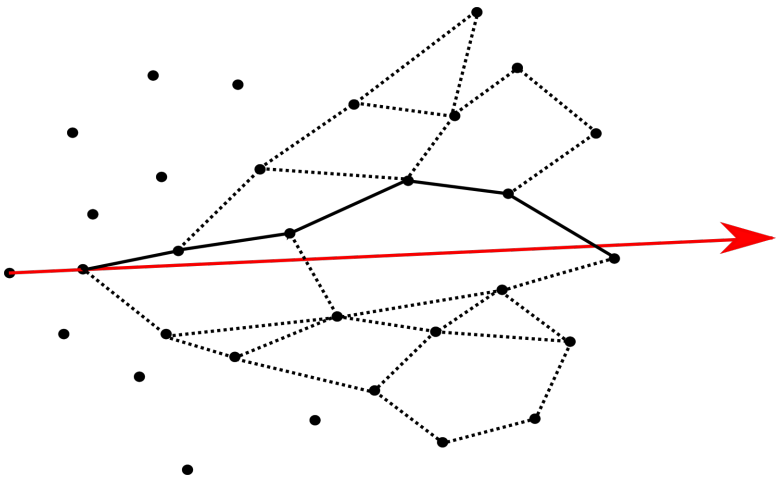

Figure 3.2: A package of photons is send through the first Delaunay line of which the direction is depicted by the red arrow. The full black lines make up the path which has the highest probability to be followed. The dotted lines represent line choices with lower probabilities. Combined, a cone is formed in the direction of the initial Delaunay line.

3.3 Ray tracing

After convergence has been reached, the line-of-sight photons are determined and a 3D image cube is created from photons which have escaped the surface of the object. The user provides all necessary information such as the distance to, orientation of and systemic velocity of the object. As well as the image resolution, units of flux and the width of the velocity bins. For the ray tracing, pixel-sized lines-of-sight penetrate the object rather than moving along the Delaunay lines. These lines-of-sight move through the Voronoi cells, for which all physical information is stored in the corresponding grid point. Thus, it is just a matter of determining through which Voronoi cell the line is passing. The step size along the line-of-sight is taken as a fraction of the Voronoi cell in order to avoid stepping over a cell. The velocity between grid points is interpolated to attain a velocity at each step along the line-of-sight. A 3D intensity cube with two spatial axes and one spectral axis, the velocity, is the output of `LIME`.

CHAPTER 4

Geometry

Our structure consists of a central star, a rotating disk around it and a bipolar outflow which is collimated by the dusty disk. This structure is defined in an analytic way. The next two sections will discuss the overall geometry of the disk and wind, what analytic functions are used, how they are derived, what assumptions are made and how realistic the models are.

4.1 Disk geometric model

The mathematical description of our disk model is formulated in a cylindrical coordinate system with use of following notation,

$$r = \sqrt{x^2 + y^2} \tag{4.1}$$

$$z = z \tag{4.2}$$

The disk is assumed to rotate according to the Keplerian velocity law, not only the midplane of the disk but the entire structure,

$$v(r) = \sqrt{\frac{GM_\star}{r}}. \tag{4.3}$$

Here G is the gravitational constant and $M_\star$ is the mass of the central star. We assume the object to be a thin, passive disk. Thin, such that it is isothermal in the vertical direction. Passive, meaning that the disk derives most of its luminosity from reprocessed star light. Active disks on the other hand, are mostly powered by the gravitational release of energy due to inward flows

of gas. With other words, they represent accretion disk. Hence, the temperature profile only has a radial dependence and will be represented by a power law

$$T(r) = T_\star \left(\frac{r}{R_\star} \right)^{-q}. \tag{4.4}$$

Here $R_\star$ and $T_\star$ are the radius and effective temperature of the star. The density distribution of the disk can be decomposed in a radial and a vertical component,

$$\rho(r, z) = \rho_c R(r) Z(H(r), z) \tag{4.5}$$

with $\rho_c \equiv \rho(r_c, 0)$ an initial density value at some characteristic distance r_c and

$$R(r) = \left(\frac{r}{r_c} \right)^{-p} \tag{4.6}$$

$$Z(H(r), z) = \exp \left[\frac{-z^2}{2H(r)^2} \right] \tag{4.7}$$

$$H(r) = H_c \left(\frac{r}{r_c} \right)^{h} \tag{4.8}$$

where $H_c \equiv H(r_c)$ an initial scale height at some characteristic distance r_c.

4.1.1 Vertical density profile

The vertical density profile of a thin disk is determined from the assumption of hydrostatic equilibrium,

$$\frac{dP}{dz} = -\rho g_z \tag{4.9}$$

with P the pressure of the gas, ρ the density of the gas along the vertical axis and g_z the vertical component of stellar gravity. Any contribution of self gravitation of the disk is ignored, which is justified if the disk is not too massive. The vertical component of the gravity on a segment of gas at a distance d from the star and a height z above the disk plane, as illustrated in Figure 4.1, is given by:

$$g_z = \frac{GM_\star}{d^2} \sin \alpha = \frac{GM_\star}{d^3} z. \tag{4.10}$$

For a thin disk ($z \ll r \rightarrow d \approx r$)

$$g_z = \frac{GM_\star}{d^3} z \approx \frac{GM_\star}{r^3} z = \Omega^2 z \tag{4.11}$$

with $\Omega = \sqrt{\frac{GM_\star}{r^3}}$ the Keplerian angular velocity.

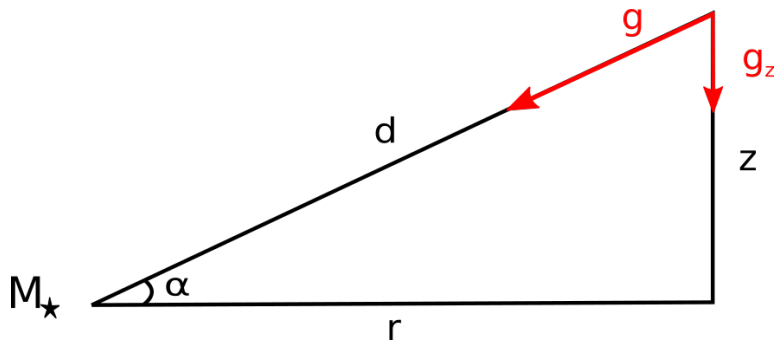

Figure 4.1: Geometry for the calculation of hydrostatic equilibrium of a point at radial distance r and height z subjected to a gravity g from a star with mass $M_\star$.

The assumption of the disk being vertically isothermal gives an equation of state $P = \rho a^2$ with a the isothermal sound speed. Hence, equation (4.9) becomes

$$a^2 \frac{1}{\rho} \frac{d\rho}{dz} = -\Omega^2 z \tag{4.12}$$

which has a solution

$$\rho(r, z) = \rho(r, 0) e^{-z^2/2S(r)^2} \tag{4.13}$$

with $\rho(r, 0)$ the density at the midplane and where $S(r)$, the vertical scale height (the distance at which the density has dropped by a value $1/e$) is given by,

$$S(r) = \frac{a(r)}{\Omega(r)}. \tag{4.14}$$

Remark that also the isothermal sound speed,

$$a(r) = \sqrt{\frac{k_B T(r)}{\mu m_H}} \tag{4.15}$$

has a radial dependence as the temperature changes radially. Here k_B represents the Boltzmann constant and μ the mean molecular weight of the gas in units the mass of a hydrogen atom m_H. We can parameterize the sound speed as

$$a \propto r^{-\beta}, \tag{4.16}$$

giving a radius dependency of the scale height:

$$S(r) \propto r^{-\beta+3/2}, \tag{4.17}$$

where the 3/2 comes from the angular velocity. This will make the disk flare, the aspect ratio $S(r)/r$ increases with increasing radius, if $\beta < 1/2$.

Combining equations (4.4), (4.15) and (4.16), a relation between β and q can be found:

$$a \propto T^{1/2} \propto r^{-q/2} \propto r^{-\beta}. \tag{4.18}$$

Thus $\beta = q/2$, meaning the disk will flare for a temperature profile $T \propto r^{-1}$ or shallower. We can therefore write the scale height $S(r)$ as a radial power law,

$$H(r) \equiv H_c \left(\frac{r}{r_c}\right)^h \tag{4.19}$$

with $h = -q/2 + 3/2$.

4.1.2 Radial density profile

The surface density is defined as the integral of the mass volume density $\rho(r, z)$ over the vertical disk height z,

$$\Sigma(r) \equiv \int_{-\infty}^{\infty} \rho(r, z)dz = \int_{-\infty}^{\infty} \rho(r, 0)e^{-z^2/2H(r)^2}dz = \sqrt{2\pi}H(r)\rho(r, 0). \tag{4.20}$$

This can be used to obtain the value for the density at the midplane,

$$\rho(r, 0) = \frac{\Sigma(r)}{\sqrt{2\pi}H(r)}. \tag{4.21}$$

The radial dependent volume density in the midplane $\rho(r, 0)$ can be obtained by assuming a power law dependence of $\Sigma(r)$,

$$\Sigma(r) = \Sigma_c \left(\frac{r}{r_c}\right)^{-f}. \tag{4.22}$$

Here Σ_c is the initial value of the surface density at a characteristic radius r_c. Using Eq. (4.19) the density profile in de midplane of the disk can therefore be represented by:

$$\rho(r, 0) = \frac{\Sigma_c}{\sqrt{2\pi}H_c} \left(\frac{r}{r_c}\right)^{-(f+h)}. \tag{4.23}$$

To have an idea of how realistic surface density profiles look like, we have to fit observationally acquired data. Unfortunately, not much work has been done in disks of AGB stars as they are recently discovered. However, as disk theory is universal and lots of research has been done in proroplanetary disks, we will take a leap of faith and continue with observationally determined results of the latter. Later, we will demonstrate that these results do not contradict the few ones found in post-AGB disks.
One specific profile of $\Sigma(r) \propto r^{-3/2}$ can be determined by an estimate of the amount of gas that was present in the protoplanetary disk of our Solar

System. The observed masses and composition of our planets can be used to derive a lower limit of the total amount of gas present at the formation of these planets. This is known as the Minimum Mass Solar Nebula (Weidenschilling, 1977). The normalisation constant depends on the convention used. The most common value used, is the one determined by Hayashi (1981) which gives a surface density

$$\Sigma(r) = 1.7 \cdot 10^3 \left(\frac{r}{AU}\right)^{-3/2} \qquad \text{g cm}^{-2}. \tag{4.24}$$

Integrating upto Neptune's distance, 30 AU, gives a lower mass of $0.01 M_\odot$ for our protoplanetary disk. This is comparable to typical estimates of protoplanetary disks around other stars (Andrews et al., 2010) which justifies this particular power law. Remember that this is still a lower limit and not an estimate of the disk when the Solar System formed, nor is the $r^{-3/2}$ dependence necessarily the actual density profile of the disk. Generally, when the surface density is characterized as a pure power law $\Sigma \propto r^f$, the value of f lies between between 0 and 1 (Mundy et al., 1996; Lay et al., 1997; Wilner et al., 2000; Kitamura et al., 2002; Andrews & Williams, 2007). A more complex model that describes viscous accretion disks (e.g. Lynden-Bell & Pringle, 1974; Hartmann et al., 1998), so-called α-disks, represent the surface density by a exponentially truncated power law,

$$\Sigma(r) = (2-\gamma)\frac{M_d}{2\pi r_c^2}\left(\frac{r}{r_c}\right)^{-\gamma} \exp\left[-\left(\frac{r}{r_c}\right)^{2-\gamma}\right] \tag{4.25}$$

where M_d is the mass of the disk, r_c a characteristic radius that indicates where the profile begins to steepen significantly from a power law, γ specifies the radial dependence of the viscous disk where the viscosity $\nu \propto r^\gamma$. Andrews et al. (2009, 2010) found a mean value of $\langle\gamma\rangle = 0.9$ for a large sample of disks. Davis (2005) found a value of $\gamma = 0.5$ for surface density of our Solar System. The most important remark is that all determined surface density profiles, either pure power law or truncated power law, are less steep than the one determined by the Minimum Mass Solar Nebula method.

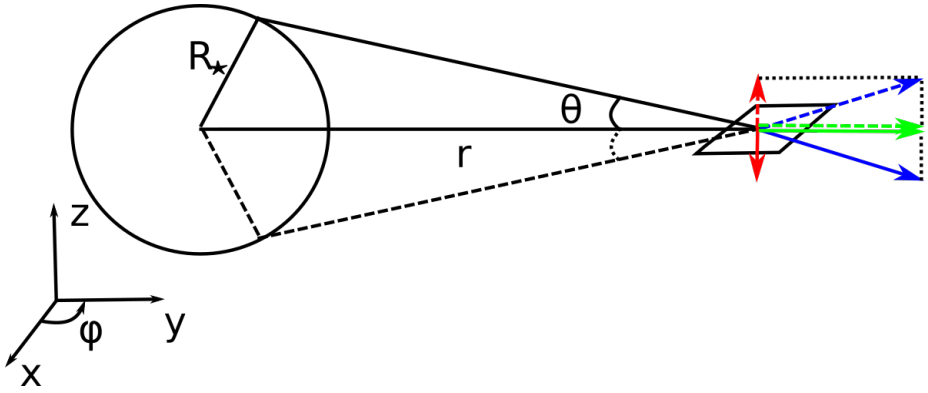

Figure 4.2: Geometry for the calculation of the flux through a surface element, at a radial distance r from a star with radius $R_\star$, of a flat, passive disk.

4.1.3 Temperature profile

Consider the most simple model, i.e. a flat disk that absorbs all the incident radiation and re-emits it as a single temperature black body. Here, back-warming of the star due to the disk is not taken into account. Consider a surface element of the flat disk, as illustrated in Figure 4.2. The total flux through this element is given by

$$F = \int I_\star \mathbf{n} d\Omega \tag{4.26}$$

where $\mathbf{n}$ is the normal to the surface element. Assuming the specific intensity (integrated over all frequencies) of the star $I_\star$ is isotropic and noting that by symmetry the x and z component equal zero (due to cancellation as can be seen on Figure 4.2), the total flux can be stated as:

$$F = I_\star \int \sin\theta \sin\phi d\Omega \tag{4.27}$$

Using the integrating boundaries that cover the whole star and $d\Omega = \sin\theta d\theta d\phi$, this becomes

$$F = I_\star \int_0^\pi \sin\phi d\phi \int_{\sin^{-1}(-R_\star/r)}^{\sin^{-1}(R_\star/r)} \sin^2\theta d\theta. \tag{4.28}$$

Which evaluates to

$$F = 2I_\star \left[\sin^{-1}\left(\frac{R_\star}{r}\right) - \left(\frac{R_\star}{r}\right)\sqrt{1-\left(\frac{R_\star}{r}\right)^2} \right]. \tag{4.29}$$

For a black body with an effective temperature $T_\star$, the specific intensity $I_\star = \frac{\sigma}{\pi} T_\star^4$, with σ the Stefan-Boltzmann constant. As the disk emits all the

incident radiation as a black body with a flux $F = 2\sigma T_{\rm disk}$, where the factor 2 arises as the disk emits from its upper and lower side. This gives a radial temperature profile of the disk,

$$\left(\frac{T_{\rm disk(r)}}{T_\star}\right)^4 = \frac{1}{\pi}\left[\sin^{-1}\left(\frac{R_\star}{r}\right) - \left(\frac{R_\star}{r}\right)\sqrt{1-\left(\frac{R_\star}{r}\right)^2}\right]. \tag{4.30}$$

As this is no simple radial dependence, a Taylor series on the right hand side is performed far from the central star ($r \gg R_\star$).

$$\left(\frac{T_{\rm disk(r)}}{T_\star}\right)^4 = \frac{1}{\pi}\left[\frac{2R_\star^3}{3r^3} + O\left(\frac{1}{r^5}\right)\right] \tag{4.31}$$

which gives a radial dependence of the disk temperature,

$$T_{\rm disk(r)} \propto r^{-3/4} \tag{4.32}$$

for the extreme case of a flat, passive disk. According to equation (4.18) where $\beta = q/2$, this give a radial dependence for the sound speed

$$a(r) \propto r^{-3/8}. \tag{4.33}$$

When also assuming that the disk is isothermal in the vertical direction, the ratio of the scale height with respect to the radius is given by a

$$\frac{H(r)}{r} \propto r^{1/8} \tag{4.34}$$

radial dependence. This means that for the case of a flat disk, the outer edges will start to show flaring. A flared disk will intercept more stellar radiation, leading to a higher temperature. Hence, a radial temperature profile of

$$T_{\rm disk(r)} \propto r^{-3/4} \tag{4.35}$$

is the steepest we would suggest for a thin, passive disk.

The temperature profile for a flared passive disk can be computed by the same way as for the flat passive disk. Namely by evaluating the flux via integration of Eq. (4.26) over the stellar surface and accounting for the correct projecting of the disk element due to the flared shaped. This is conceptually not that difficult but requires some complex geometric transformations. An exact calculation can be found in the appendix of Kenyon & Hartmann (1987). At large radii, they find that the disk approaches a temperature profile

$$T_{\rm disk} \propto r^{-1/2} \tag{4.36}$$

which is less steep than previously determined for a flat passive disk. A different approach was performed by Chiang & Goldreich (1997), which is valid at large distance $r \gg R_\star$ and considers the star as a point source. The incident radiation is absorbed at a radial distance r in the midplane and a height H_p. Note that this height is not the same as the scale height as H_p is determined by the opacity, ergo optical depth, of the beam of light and not directly by the vertical density structure of the disk. The beam of light hits the disk surface at $\tau = 1$ but this is not necessarily at the scale height H. For this reason, it is impossible to state at what scale height the surface of the disk is reached. From the geometry of Figure 4.3 we define an angle α as the difference between the radial slope of the actual disk the slope that the incident radiation makes when it hits the disk,

$$\alpha \equiv \frac{dH_p}{dr} - \frac{H_p}{r}. \tag{4.37}$$

The total amount of flux that reaches a surface element at a radial distance r is

$$F_{tot} = \frac{L_\star}{4\pi r^2} \tag{4.38}$$

When considering that the surface element is slanted by an angle α, this translates to

$$F_{elem} = \frac{L_\star}{4\pi r^2} \sin\alpha \approx 2\alpha \frac{L_\star}{4\pi r^2} \tag{4.39}$$

where the last equality assumes the angle α to be small. Assuming again that the disk reradiates as a black body, with a flux $F = \sigma T_{disk}$, the disk surface temperature profile goes as,

$$T_{disk} = \left(\frac{L_\star}{4\pi r^2}\right)^{1/4} \alpha^{1/4} r^{-1/2}. \tag{4.40}$$

Since $L_\star = 4\pi\sigma R_\star^2 T_\star^4$, an equivalent expression is

$$T_{disk} = T_\star \alpha^{1/4} \left(\frac{r}{R_\star}\right)^{-1/2} \tag{4.41}$$

which is that same radial dependence as Kenyon & Hartmann (1987) acquired. Because the radiation only hit the surface of the disk, this temperature profile only holds for the surface. But as done before, we can assume the disk to be vertically isothermal such that Eq. (4.41) is valid inside the whole disk. It is reasonable to assuming that H_p is only a few times H, as the Gaussian vertical density only starts to drop steeply at z larger than H.

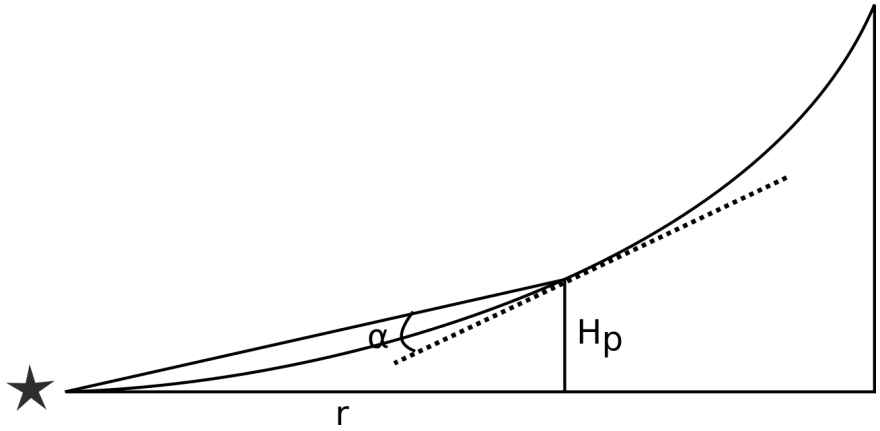

Figure 4.3: Geometry for the calculation of the radial temperature profile of a flared disk. At a distance $r \gg R_\star$ the stellar radiation gets absorped at a height H_p above the midplane. The angle α is the difference between the tangent to the disk and the slope of the incident radiation.

During these derivations a lot of assumptions were made, not all equally realistic. The assumption of vertical isothermality is anything but realistic. A more correct representation of a disk is depicted in Figure 4.4. The inner regions are cooler than the outer areas as they are shielded from incident radiation. Secondly, the assumption that the disk emits as a black body is too simple. The surface layers radiate at a higher temperature than the lower layers. This is because these upper layers are more efficient at absorbing stellar radiation than emitting. Dust particles with a radius a are good at absorbing radiation with wavelengths $\lambda < 2\pi a$ but inefficient at absorbing and emitting radiation with wavelengths $\lambda > 2\pi a$. When a dust particle is in radiative equilibrium, the radiative transfer equation integrated over all frequencies equals zero,

$$\int_0^\infty \frac{dI_\nu}{ds} d\nu = \int_0^\infty \frac{j_\nu}{4\pi} - \alpha_\nu I_\nu d\nu = 0 \tag{4.42}$$

with j_ν and χ_ν the emission and extinction coefficients respectively. When we assume the radiation is isotropic, $I_\nu = J_\nu$, and the particle is in local thermodynamic equilibrium, $S_\nu \equiv j_\nu / 4\pi\alpha_\nu = B_\nu(T)$, where S_ν is the source function and $B_\nu(T)$ a *Planck* curve at a certain temperature, this becomes:

$$\int_0^\infty \alpha_\nu [S_\nu - J_\nu] d\nu = 0 \tag{4.43}$$

$$\int_0^\infty \alpha_\nu J_\nu d\nu = \int_0^\infty \alpha_\nu S_\nu d\nu \tag{4.44}$$

This equation describes that the total amount of energy absorbed by an individual dust grain per second (LHS) must be equal to the total energy

emitted by that particle per second (RHS). The extinction coefficient can be expressed as

$$\alpha_\nu = n_d \sigma_d(\nu) = n_d \pi a^2 Q_{\text{ext}}(\nu) \tag{4.45}$$

with n_d the density of the dust grain, $\sigma_d(\nu)$ the cross-section, a the radius by the grain and $Q_{\text{ext}}(\nu)$ the extinction efficiency. The extinction efficiency consists of two contributors, on the one hand absorption by the grain, on the other hand scattering of photons. As the scattering component does not play a role in the thermal balance, we will omit this. If one assumes that the grain absorbs and emits as a black body, the extinction efficiency is unity for all frequencies. But a more realistic view is described by *Mie theory* (Mie, 1908; Debye, 1909) where the most important factors are the dimensionless size parameter

$$x = \frac{2\pi a}{\lambda} \tag{4.46}$$

and the complex refractive index of the grain

$$m = n - ik \tag{4.47}$$

where n is a measure for scattering and k determines the absorption cross-section. Mie theory however still assumes the grains to be spherical. In general for $\lambda_{phot} \gg a$ the absorption coefficient goes as $Q_{abs} \propto \lambda^{-p}$ with $p = 1$ for $1 < \lambda < 30\mu$m and $p = 2$ for larger wavelengths. For $\lambda_{phot} \ll a$ the coefficient is of the order of unity, $Q_{abs} \propto 1$. Hence, grains with typical sizes of $0.01 - 0.1\mu$m absorb ultraviolet and optical wavelengths quite easily. When the wavelength is much larger than the grain size, the radiation hardly 'notices' the grain and therefore no radiation is absorbed. According to *Kirchoff's law*: $j_\nu/4\pi = \alpha_\nu I_\nu$ (Eq. (4.42) at thermal equilibrium) also hardly any radiation will be emitted at this wavelength. Plugging Eq. (4.45) into equation (4.44) results in:

$$\int_0^\infty Q_{\text{ext}}(\nu) J_\nu d\nu = \int_0^\infty Q_{\text{ext}}(\nu) B_\nu(T_d) d\nu. \tag{4.48}$$

The total amount of energy at both hand sides need to be the same but inefficient cooling at long wavelengths, $Q_{abs} \propto \lambda^{-2}$, decreases the planck curve at this wavelengths. Hence, the area under the emitting planck curve, which represents the total energy, reduces leading to an inequality of both hand sides. To increase this area again, the peak of this curve needs to shift towards shorter wavelengths by increasing the temperature, as determined by Wien's displacement law. Hence, in order to compensate for the more efficient heating due to optical and ultraviolet light and inefficient cooling at long wavelengths the temperature of the dust grain must be higher than as it would absorb and emit as a black body. Therefore, in the more complete description, the surface layers of the disk, which absorb the stellar radiation, cannot be considered as a simple black body.

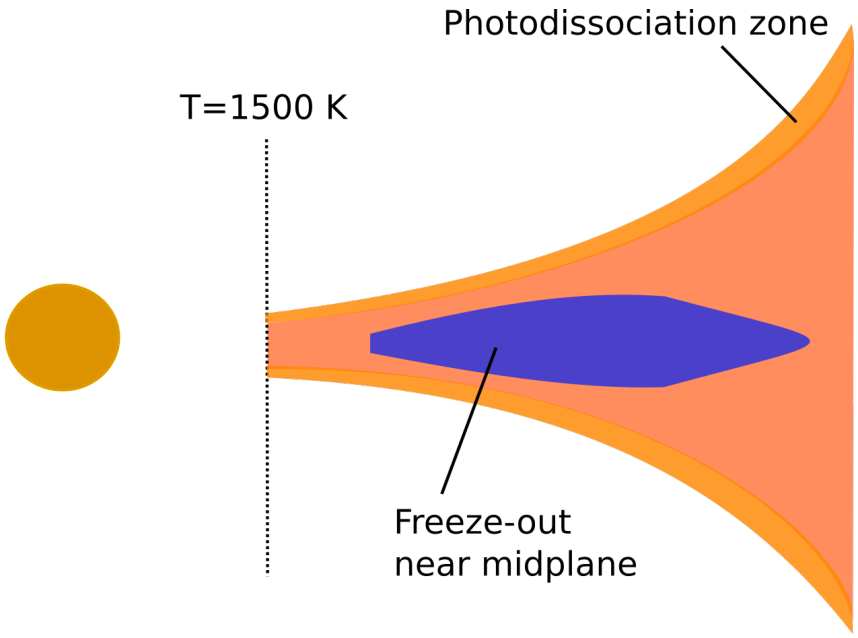

Figure 4.4: A more realistic illustration of a disk which starts at condensation temperature $T = 1500$ K. The inner regions of the disk get less heated and a zone around the midplane arises where molecules freeze into ices. The most upper layes of the disk are bombarded with photons such that molecules start to photodissociate.

4.1.4 Summary

Our disk rotates entirely Keplerian,

$$v(r) = \sqrt{\frac{GM_\star}{r}} \tag{4.49}$$

with an overall volume density profile:

$$\rho(r,z) = \rho_c \left(\frac{r}{r_c}\right)^{-p} \exp\left[\frac{-z^2}{2H(r)^2}\right] \tag{4.50}$$

where

$$H(r) = H_c \left(\frac{r}{r_c}\right)^{h}. \tag{4.51}$$

For a surface density and temperature profile,

$$\Sigma(r) = \Sigma_c \left(\frac{r}{r_c}\right)^{-f} \tag{4.52}$$

$$T(r) = T_\star \left(\frac{r}{R_\star}\right)^{-q} \tag{4.53}$$

the relations

$$p = f + h \tag{4.54}$$

$$h = -\frac{q}{2} + \frac{3}{2} \tag{4.55}$$

hold. Here, ρ_c and H_c are the density in the midplane and the scale height respectively, at some critical radius r_c. Note that only f determines amount of flaring of the disk. Together with q, these parameters are the only ones that determine the morphology of the disk. Therefore, the temperature and the surface density are disentangled physical quantities that determine the disk morphology. Equations (4.50), (4.52) and relation (4.54) indicate the importance of the radial dependence of surface density profile $\Sigma(r)$.

4.2 Wind geometry

For describing the wind geometry, it is easiest to work in spherical coordinates,

$$r = \sqrt{x^2 + y^2 + z^2} \tag{4.56}$$

$$\theta = \cos^{-1}\left(\frac{z}{r}\right) \tag{4.57}$$

$$\phi = \tan^{-1}\left(\frac{y}{x}\right). \tag{4.58}$$

For a spherical mass loss of the star, assuming that the amount of matter lost through each shell is the same, the mass continuity equation is given by:

$$\frac{dM}{dr} = 4\pi r^2 \rho(r). \tag{4.59}$$

For a more general volume the solid angle Ω, which equals 4π for a sphere, comes into play

$$\frac{dM}{dr} = \Omega r^2 \rho(r). \tag{4.60}$$

The mass loss rate $\dot{M}$ then becomes:

$$\frac{dM}{dt} = \frac{dM}{dr}\frac{dr}{dt} = \Omega r^2 \rho(r) v(r). \tag{4.61}$$

When the mass loss rate and the velocity profile of the star are known, the density in each point of the wind can be calculated via

$$\rho(r) = \frac{\dot{M}}{\Omega r^2 v(r)}. \tag{4.62}$$

The velocity profile of a mass losing star is often parametrized by a *β-law*. For a star having some initial wind velocity v_0 and a terminal velocity v_∞, this β-law is given by,

$$v(r) = v_0 + (v_\infty - v_0)\left(1 - \frac{r_c}{r}\right)^\beta \tag{4.63}$$

with β a variable value and r_c the radius at which the wind starts to accelerate. As the acceleration is driven by dust-gas interaction, r_c is the distance where the dust starts to form, also known as the dust condensation radius. The temperature profile of a stellar wind is often described by a power law,

$$T(r) = T_\star \left(\frac{r}{R_\star}\right)^{-s}, \tag{4.64}$$

with s some exponent.

4.3 Boundary conditions

4.3.1 Edge of the disk

The most correct method to distinguish between what is disk and what is wind, is to examine the density in each point. Each side of the interface between disk and wind should have the same density, as an abrupt change is unrealistic. So both wind and density profiles are evaluated in each grid point and the profile which gives rise to the largest density, determines the region this point represents. This density criterion separates the disk from the wind region, each with its own physical quantity profiles. However, this introduces issues for extreme mass loss rate/disk mass combinations. A strong wind, small disk combination will enable the wind to completely obliterate the disk. Even for higher disk masses, the far end of the disk will have much lower densities than the wind density profile yields. This is because the wind density only drops as $1/r^2$, while the disk density on the other hand, drops in the midplane alone already as $1/r^{2.25}$, it then drops in the height again as a Gaussian distribution. This will render a disk whose outer regions turns into wind regions. This might be possible as the wind will shear along the edges and at the outer end engulf the disk by turbulent motion. Such engulfment of the disk by the wind might be possible, depending on the formation mechanism of the disk. As the disk slowly gets consumed by the wind, turbulent instabilities will arise at the interfaces. However, it is beyond the scope of this research to simulate turbulent behaviour due to disk-wind interaction.
We therefore propose to use a geometrical criterion to separate disk and wind. Again, a definition for the 'edge of the disk' is needed. A possible approach is the height at which the incident radiation of the star reaches optical depth

$\tau = 1$, as discussed for the temperature profile of a flaring disk (Eq. 4.41). In that case however, no mass loss through a wind was considered as opposed to here, where the radiation needs to penetrate additional dense regions. As discussed earlier, this height H_p will probably be a few times the scale height H. We empirically determined that $H_e(r) = 1.4H(r)$ is a good estimate for the edge such that it resembles the density criterion for the parameter combinations for which no complications arise. For this value the density difference between disk and wind is not immensely abrupt. We define an angle α which separates the disk from the wind region:

$$\alpha = \tan^{-1}\left(\frac{r_f}{1.4H_f}\right) \tag{4.65}$$

where r_f is the radius of the entire disk and $H_f \equiv H(r_f)$ is the scale height at this radius which is calculated via Eq. (4.51) with H_c the scale height, calculated via its definition, at r_c with temperature T_c. Using this criterion, the flared shape of the disk is preserved upto a scale height $H_p(r) = 1.4H(r)$. Figure 4.5 illustrates the choice of the geometric disk edge. This limited disk contains 83.85% of the total mass of the disk. The geometrical wedge-shaped disk region, within α, contains 94.31% of the disk mass.
As only about 5% of the total disk mass is cut off using α and differences between wind and disk densities at this boundary are small, our geometrical separation is justified.

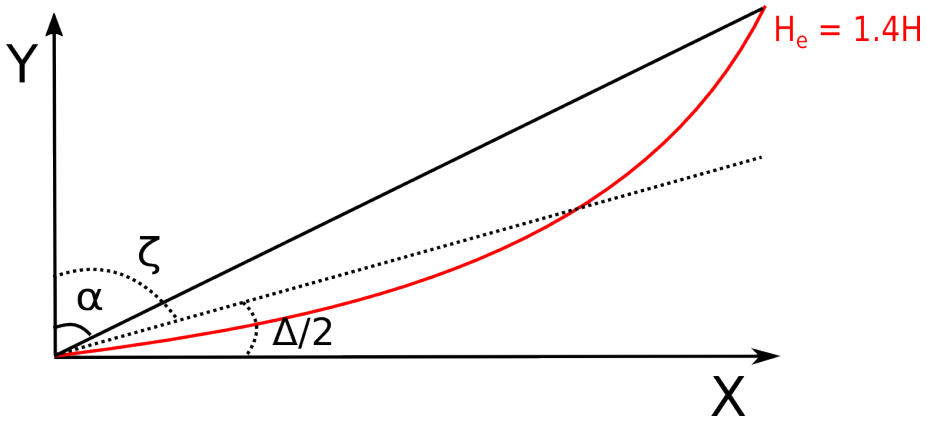

Figure 4.5: A graphical representation of the geometrical separation of disk and wind by an angle α. The velocity transition zone is determined by the angle ζ.

4.3.2 Velocity field

Up till this point, we have always assumed the disk to be rotating completely Keplerian. This brings about a problem at the interface between disk and

wind. The radial velocity component of the wind abruptly disappears as we enter the disk at $\theta = \alpha$. It is inconceivable that such a radical change in velocity occurs in real life objects. The wind will shear against the low density outer edges of the disk and blow it partially or completely away. Due to the difference in shear velocity, it is quite probable that vortices will arise, better known as Kelvin-Helmholtz instabilities. When looking at the object face-on, the disk's emission will only contribute to the velocity bin $v = 0$ km/s. As the disk fills up a substantial part of the volume, the smaller projected components of the radial wind are not reached thus creating a gap in velocity space.
Therefore we propose to impose a smooth transition between the wind and disk velocity profiles. As the density of the disk increases, the wind will have less success at blowing outer parts of the disk away. We will assume that the radial wind velocity decreases as it 'enters' the disk. Still, several scenarios are possible, the steepness of the decline and where the wind contribution completely disappears are two crucial aspects. For this approach, it is important to where the 'edge' of the disk is defined. We will use the wind-disk separation according to α as stated above. We composed a normalized smoothing function $F(\theta)$ that is multiplied with the radial velocity profile of the wind,

$$F(\theta) = \left| \frac{2}{e^{k(\theta-\zeta)} + 1} - 1 \right| \qquad \theta < \zeta \tag{4.66}$$

$$F(\theta) = \left| \frac{2}{e^{k(\theta-\zeta-\Delta)} + 1} - 1 \right| \qquad \theta > \zeta + \Delta \tag{4.67}$$

where ζ is the angle at which the radial wind velocity component disappears completely, $\Delta = \pi - 2\zeta$ is the part which is still completely Keplerian and k is determines the steepness of the function. A schematic representation of this transition zone is illustrated in Figure 4.5. We choose k such that $F(\alpha) = 0.99$ where α is the angle which represents the edge of the disk. This smoothing function is depicted in Figure 4.6. There now only rests us the choice what fraction of the disk remains 100% Keplerian. It is reasonable to assume that only 10% to 20% of the disk will be penetrated by the wind. But as we have the opportunity to also probe the more extreme cases, we will analyse disks with fractions of 100%, 90%, 80%, 50% and 0% which have Keplerian velocity profiles. The residual fraction of the disk is a superposition of a Keplerian and radial velocity component. The latter, extreme cases might be possible for high mass loss rates and low disk masses. But then arise the questions: "Can we still speak of a disk?" and "How can low mass disks be establish with such high mass loss rates?". It is possible that the disk may have been formed during a stage of less violent mass loss and due to a sudden event which increases the mass loss rate of the star, this disk might experience heavy wind bombardment penetrating its most inner layers.

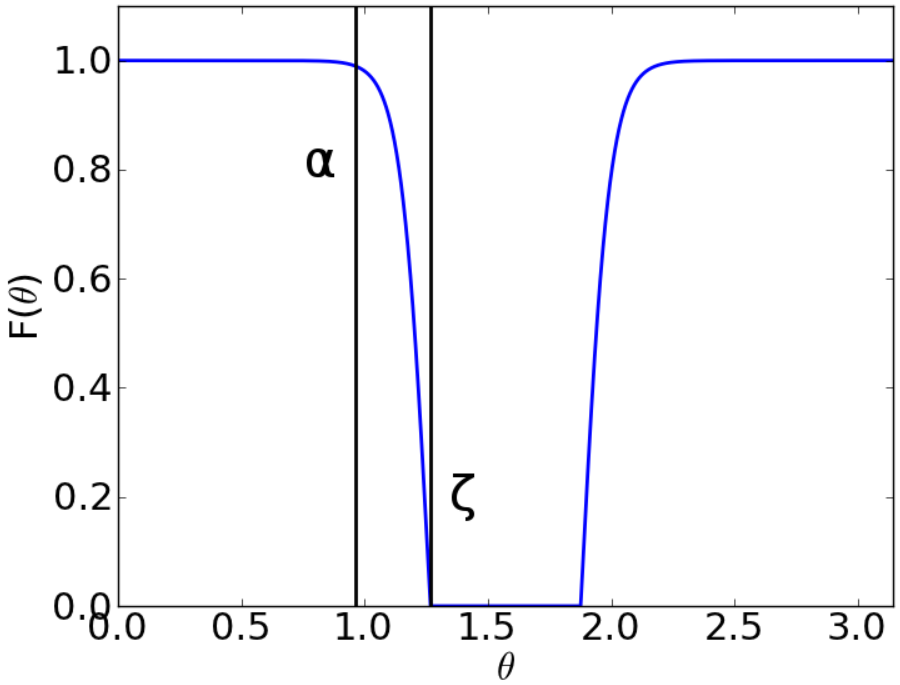

Figure 4.6: The smooting function $F(\theta)$ for a transition zone which comprises 50% of the disk with $\alpha = 55°$ and $\zeta = 73°$.

Chapter 5

Model assumptions

In order to have realistic simulations, typical values for physical en stellar parameters are used. Our object will have a mass, $M_\star = 2M_\odot$, a radius $R_\star = 2$ AU and an effective temperature $T_\star = 2500K$, which are typical values for an AGB-star. The mass loss will span between 10^{-7} $M_\odot$ yr^{-1} and 10^{-5} $M_\odot$ yr^{-1}. More extreme cases are not useful for our analysis as too high mass loss rates will dwarf the flux contribution of the disk, nullifying our main goal. Moreover, these more extreme cases will not contribute to differentiating disk/wind morphologies hence providing no additional useful material.

We have empirically determine that the a β-law velocity does not enrich our output with new insights. In the PV-diagrams, a β-law is indistinguishable from a constant velocity profile. The β-law only contributes in a minor way to low velocities, which are not probed for the constant velocity, in the line profile. The evolution of a β-law, for a much used value of $\beta = 0.5$, is illustrated in Figure 5.1. As this rapidly reaches roughly a constant value, it is clear that its contribution to low velocities is minor. Even though the density is much higher in the inner parts, the outer part contribution is more prominent as the density goes as $1/r^2$ but the emitting volume roughly goes as r^3, making to volume more decisive. Small β exponent however, will contribute more substantially to lower velocity and as we do not know the exact value of this component, this should be kept in mind. To keep our model as simple as possible, we opt for a constant wind velocity. As dust driven AGB-winds have a terminal velocity of the order of 10 km/s, we adopt an arbitrary value of $v = 15$ km/s. To account for turbulent motion in the stellar outflow, a global turbulent velocity of 1.0 km/s is presumed.

The temperature throughout the wind will decrease as a power law, according to equation (4.64) with a much used value of $s = 0.5$. The wind loss of our object will not be spherically symmetric but, due to the dusty disk around our stellar object, it will be collimated in a double cone. The corresponding solid angle for this geometry is $\Omega = 4\pi(1 - \cos(\delta))$ with δ the angle which denotes the inner angle of the cone.

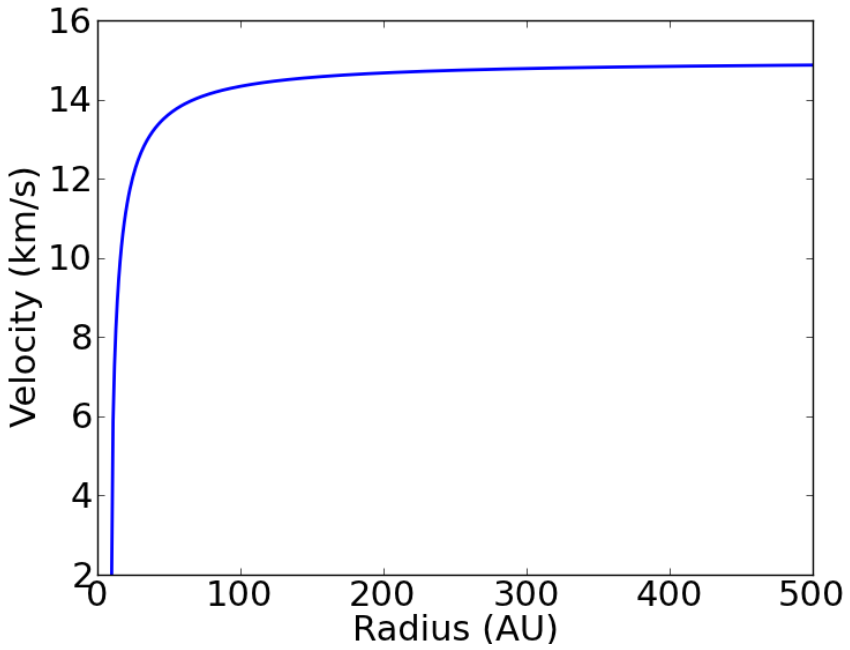

Figure 5.1: A β-law starting at $r = 10$ AU with $\beta = 0.5$.

As stated before, the temperature profile is a determining factor for the shape of the disk. The parameter q, in equation (4.53), adopts a value of 0.75 for the flat disk limit and a value of 0.5 for the more complex, flaring shape. As Hartmann et al. (1998) and Chiang & Goldreich (1997) showed, the latter is more consistent with reality, a fixed value of $q = 0.5$ will be used as a power law exponent for the disk temperature profile. As a consequence the scale height of the disk will increase with a power law exponent $h = -q/2 + 3/2 = 1.25$ in Eq. (4.51).
Besides the temperature, it is the surface density that determines the overall volume density profile of the disk. In the previous section, we argued that a number of different radial dependent surface density profiles are fitted to observations. A simple power law, Eq. (4.22), or a exponentially truncated power law, Eq. (4.25), and for each a wide variety of power law exponents. To not make the model needlessly complex, from this point forward, an ordinary power law will be used. The exponent can be varied from $f = 0.5$

upto $f = 1.5$ to check its impact on the observables. The lower limit is semi-arbitrary and justified as follows: imagine a negative exponent is used, this implies that the density is increasing outwards whereby the disk has much more material in its outer regions than in its inner ones. This is counter-intuitive and not what we aspire. A negative exponent may be suitable for disks which have formed gaps, most likely due to planet formation. This may be relevant for proto-planetary disks, but not the AGB-disks we are focussing on. To that end, no negative power law exponents will be useful. Another possible lower limit is assuming the surface density is constant within the disk, $f = 0$. But again, this implies the disk has more material in its outer layers as compared to its inner ones. Therefore, the semi-arbitrary value of $f = 0.5$ is used as a lower limit. The upper limit value of $f = 1.5$ is justified by the Minimum Mass in Solar Nebula and the fact that no fit to observations yields a higher value, up till now. Nevertheless, we have empirically determined that the three mentioned values for f are indistinguishable in the PV-diagrams and only give a slight difference in the line profiles. To limit our parameter grid we therefore decide to only probe the value $f = 1.0$ as this is a good average of the observed ones.
Combining the temperature and surface density profiles, the volume density, according to Eq. (4.50) and equality (4.54), will decrease as a power law in the radial direction with the steepness factor $q = 2.25$. This coincides with an average of fitted density profiles of post-AGB stars and planetary nebula (Bujarrabal & Alcolea, 2013; Bujarrabal et al., 2015).

Another parameter to examine is the total mass of the disk. Bujarrabal et al. (2013) determined values between $M_{\rm disk} = 6 \cdot 10^{-3} M_\odot$ and $M_{\rm disk} = 1.2 \cdot 10^{-2} M_\odot$ for disk masses of nebula of about 1000 AU around post-AGB stars. These masses were determined from estimates of the CO rotational temperature and ^{13}CO fraction, and have an uncertainty of a factor of two. As the mass of only four disks was determined, we increase our range of the disk mass with one order on the lower and upper end. Disk masses above $0.1 M_\odot$ are gravitational unstable, which is not included in our simple model. Gravitational instability would also nullify the assumption of hydrostatic equilibrium which on its turn would completely change the density profile of the disk. This upper limit can be attain from two different perspectives. Firstly, the vertical gravitational acceleration of an infinite flat disk $g_{z,d} = 2\pi G\Sigma$. The disk is gravitationally stable is this is small compared to the stellar gravity at some height H,

$$2\pi G\Sigma < \frac{GM_\star}{r^3} H \tag{5.1}$$

$$\frac{M_d}{M_\star} \lesssim \frac{1}{2}\frac{h}{r} \tag{5.2}$$

where we used that the mass of the disk is given by $M_d = \pi r^2 \Sigma$. To get

an estimate, we use the scale height as vertical distance for a temperature around 10 K, a solar mass star and comprising a disk of radius 500 AU. This gives an order estimate of

$$\frac{M_d}{M_\star} \lesssim \frac{1}{2}\frac{h}{r} \approx 0.1 \tag{5.3}$$

as stability criterion. The same result can be achieved by comparing the free-fall time scale

$$\tau_{ff} \propto \sqrt{\frac{1}{G\rho}} \propto \sqrt{\frac{R^3}{GM_d}} \propto \sqrt{\frac{R}{\pi G\Sigma}} \tag{5.4}$$

with the time scale to destroy forming clumps by means of azimuthal shearing

$$\tau_{shear} \propto \frac{1}{R}\left(\frac{d\Omega}{dR}\right)^{-1} \propto \Omega^{-1} \tag{5.5}$$

where in both above equations R is the radius of the collapsing blob of material. We assumed a Keplerian angular rotation and again the mass of the disk is given by $M_d = \pi r^2 \Sigma$. The disk will gravitationally collapse when

$$\tau_{ff} < \tau_{shear} \tag{5.6}$$

$$\sqrt{\frac{a}{\pi G\Sigma\Omega}} < \frac{1}{\Omega} \tag{5.7}$$

$$\frac{a\Omega}{\pi G\Sigma} < 1 \tag{5.8}$$

where the left hand side of the latter equality is the Toomre parameter (Toomre, 1964). Next, this can be transformed to Eq. (5.3) justifying our upper limit of $0.1 M_\odot$.

Jeffers et al. (2014) found an inner dust density of $5.6 \cdot 10^{-19}$ g/cm^3 at 15 AU for their best SED fit to the carbon-rich AGB star CW Leo. Converting this to gas density with the commonly used gas-to-dus-ratio of $\Phi = 100$, inserting this value as ρ_c in eq. (4.50) and integrating over the whole volume, we find a disk mass of the order of $10^{-5} M_\odot$. Due to the above mentioned reasons, we will use values of $M_{\rm disk} = 1.0 \cdot 10^{-5} - 1.0 \cdot 10^{-1} M_\odot$ for the mass of the disk. Again, to limit our parameter grid we will only probe $M_{\rm disk} = 1.0 \cdot 10^{-5} M_\odot$, $1.0 \cdot 10^{-3} M_\odot$, $1.0 \cdot 10^{-1} M_\odot$, by which we do not lose any information.

For the analysis of parameter influences, the initial density ρ_c in eq. (4.50) is chosen such that the mass of the disk is the same in each situation. As the masses derived by Bujarrabal et al. (2013) are for disk sizes of a 1000 AU in diameter, we also take this same size for the disk in our model. We set it at a distance of 150 pc, based on the CW Leo which is the nearest carbon-rich ABG star (Men'shchikov et al., 2001; Groenewegen et al., 2012, and references therein), hence having a spatial coverage of 7.5 arcsec in the

plane of the sky.

In AGB stars, the fractional abundance X(^{12}CO) is found to vary between about $2 - 4 \cdot 10^{-4}$ in O-rich stars and $6 - 8 \cdot 10^{-4}$ in carbon-rich stars (e.g. Teyssier et al., 2006; Ramstedt et al., 2008, and references therein), but the ^{12}CO/^{13}CO abundance ratio is higher in carbon-rich stars, resulting in a similar value of the ^{13}CO abundance, which is usually found to be X(^{13}CO) $\approx 2 \cdot 10^{-5}$ (e.g. Kahane et al., 1992, 2000; Bujarrabal et al., 1994; Schöier & Olofsson, 2000; Schöier et al., 2011, etc.). We therefore adopt an average value X(^{12}CO)$= 5.0 \cdot 10^{-4}$ in our simulations.

Carbonaceous dusty winds mainly consist of amorphous carbon and silicon carbide, 85% and 15% respectively (Srinivasan et al., 2010, and references therein). As amorphous carbon is most abundant, its condensation temperature $T_c = 1500$ K (Hanner, 1988) will be used as a critical temperature. If silicon carbide is considered as well, according to Speck et al. (2009), the average condensation temperature will decrease a bit, depending on the gas pressure. The condensation temperature T_c determines the beginning of the disk. Via Eq. (4.4) with $q = 0.5$, we find that the disk would theoretically start at $r_c = 5.6$ AU. As a lot of assumptions were made for this particular temperature profile, even for the one of Eq. (4.36) which only holds at large distances, deriving this distance theoretically is most likely not very realistic. We therefore take an arbitrary start radius $r_c = 10$ AU, which is of the order of the ones found for the few AGB disks (Jeffers et al., 2014; Kervella et al., 2014; Lykou et al., 2015). For later purposes we assume that the scale height at that distance is determined by Eq. (4.19), just as at any other place in the disk. This is not necessarily correct as the strong radiation of the star hitting this 'wall' of high density can inflate this region substantially.

As observers do not know how their object is oriented in the sky, it is important to model our object for a range of different orientations. Rotation around the z-axis is unnecessary as our object is axisymmetric. Rotation around the y-axis denotes different inclination angles and is a necessary parameter to probe. Rotation around the x-axis however, is unnecessary as observers can choose their slice through the 3D data cube, with a certain position-angle (PA) with respect to the declination axis, such that it coincides with our fixed object. To limit the number of inclination angle but still probe the angle-space properly, six evenly spread values between $i = 0°$ and $i = 90°$ are chosen.
An overview of all parameters can be found in Tabel 5.1.

Table 5.1: Fixed model parameters

Stellar parameters	
$T_\star$(K)	2500
$R_\star$ (AU)	2.0
$M_\star$ ($M_\odot$)	2.0
Distance (pc)	150
Disk parameters	
q	0.5
f	1
CO/H_2	$5.0 \cdot 10^{-4}$
r_c (AU)	10
T_c (K)	1500
v_{turb} (km/s)	1.0
Wind parameters	
s	0.5
v_∞ (km/s)	10
v_{turb} (km/s)	1.0
Grid parameters	
$\alpha(^\circ)$	55
H_{edge}	1.4 H

Table 5.2: Variable model parameters with their labels

Parameter	Values	Labels
$\dot{M}(M_\odot/\mathrm{yr})$	$1.0 \cdot 10^{-5}$	ML5
	$1.0 \cdot 10^{-6}$	ML6 (REF, DISK, WIND)
	$1.0 \cdot 10^{-7}$	ML7
M_{disk} ($M_\odot$)	$1.0 \cdot 10^{-1}$	MD1
	$1.0 \cdot 10^{-3}$	MD3 (REF, DISK, WIND)
	$1.0 \cdot 10^{-1}$	MD1
Keplerian fraction	100%	KVZ10 (REF, DISK, WIND)
	90%	KVZ90
	80%	KVZ80
	50%	KVZ50
	0%	KVZ0
Inclination ($^\circ$)	$n \cdot 18 \; \forall \; n \in \{0, 1, 2, 3, 4, 5\}$	

Chapter 6

Results

6.1 Reference model

To accurately determine the impact of each parameter, a reference model is used to compare with. This way, degeneracy of parameter effects is limited. It is obvious to choose a combination of average parameter values as a reference. Hence, the reference object has a mass loss rate $\dot{M} = 1.0 \cdot 10^{-6} M_{\odot}/\mathrm{yr}$, a disk mass $M_{disk} = 1.0 \cdot 10^{-3} M_{\odot}$ and is assumed to fully rotate Keplerian. For simplicity, parameter values are denoted with abbreviations as stated in Tabel 5.1. For an optimum comparison, the reference model also contains all different inclination angles. This makes it possible to perceive parameter impacts as a function of the inclination angle. As it is not always possible to disentangle wind and disk contributions, a wind-only and disk-only model are simulated as well. This makes it easier to comprehend how the wind and the disk establish themselves in the PV diagrams and line profiles. This is particularly helpful for orientations not seen face- or edge-on as these are much harder to envision. The contribution of the wind and disk can then roughly be scaled to the appropriate parameter combination of mass loss rate and disk mass. The combination of average parameter values with a wind-only and disk-only simulation for all different inclination angles, makes this the optimal approach for parameter comparison.

As it is not self-explanatory to visualize the complex projected velocity profile of the disk, Figure 6.1 depicts regions with the same projected velocity as a contour plot. The figure is a view from above onto the Keplerian disk which rotates in the (x,s)-plane. The projected velocity is observed along the

s-axis, which is the line-of-sight, with the left side rotating towards us and the right side away from us. It is clear that the higher projected velocities arise from regions located in the vicinity of the central star and are elongated in the x-direction whereas lower projected velocity regions stretch to the outer regions of the disk. Note that when looking at $v = 0$ km/s, one can only see a narrow strip of the disk. The width of each contour plot depends on the size of the velocity bins used to observe.

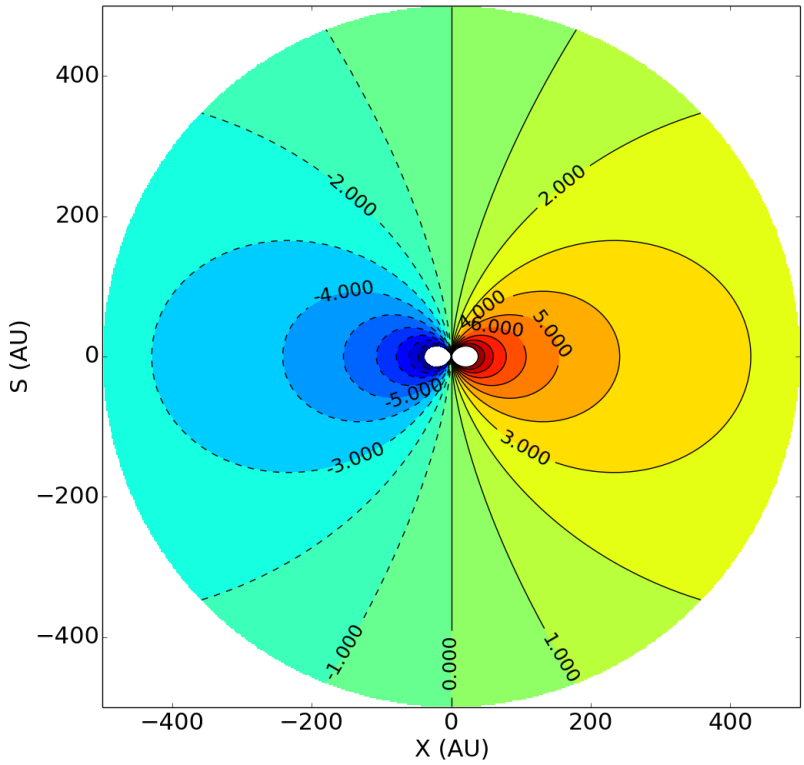

Figure 6.1: A top view of contour lines of projected velocity in the line-of-sight. The S-axis denotes the line-of-sight whereas the X-axis is the horizontal spatial axis. Negative velocities and positive velocities are towards and away from the observer respectively.

6.1.1 DISK model

The grid of PV-diagrams of this entire reference model is shown in Figure 6.8. Let us first focus on the disk, this is easiest to comprehend via the X-axis collapse because here the disk covers the whole spatial range. Each X-coordinate represents a slit, at this coordinate, through the disk in the direction of the line-of-sight. Along this slit you will encounter regions with different velocities, which can be read off from the velocity axis. All information, intensities and velocities, in this slit is then collapsed onto the line-of-sight axis.

Collapse onto X-axis

Face-on: Consider the PV-diagram $i = 0°$ where we see the disk face-on. As our disk is rotating fully Keplerian, it only rotates in the plane perpendicular to the line-of-sight. Hence, we do not see the disk rotate. This corresponds to the disk being in the $v = 0$ km/s velocity bin. As expected, on the PV-diagram, the disk is a narrow slit around zero velocity. It has some thickness as the velocity bin is 0.5 km/s wide and there is a turbulent velocity of 1.0 km/s.

The intensity decreases from $X = 0$ outwards. This can be understood with the help of the illustration in Figure 6.2, which represents a cross-section of the disk at $v = 0$ km/s. We will explain the intensity distribution in the PV-plots by means of density, volume and opacity effects. Note however, that due to mainly collisional excitations of CO, the temperature, and therefore the source function, are important factors. As we discussed before, the emitting volume is more important than the density, therefore the outer regions will contribute more to the total emission. But when collapsing onto the X-axis, around X=0 the total emission will be largest as more material, a larger volume, is collapsed onto the axis. Collapse onto larger values[1] of X, will only comprise a section of the outer edges, hence contributing less to the total emission. This is exactly what can be seen on the PV-diagram.
Zooming in onto the X=0 region, we ascertain that the maximum flux does not arise from X=0 exactly but a value a little larger. This is an optical depth effect. At some distance along the line of sight, the disk starts to become optically thick, which makes it much harder for the photons of the regions behind to escape the disk. The $\tau = 1$ level is reached the earliest for an X=0 line-of-sight as this is where the density is always highest. Figure 6.3 illustrates a possible location of the $\tau = 1$ level for this disk orientation.

[1] To keep the analysis as simple as possible, we will always talk about absolute values unless stated otherwise.

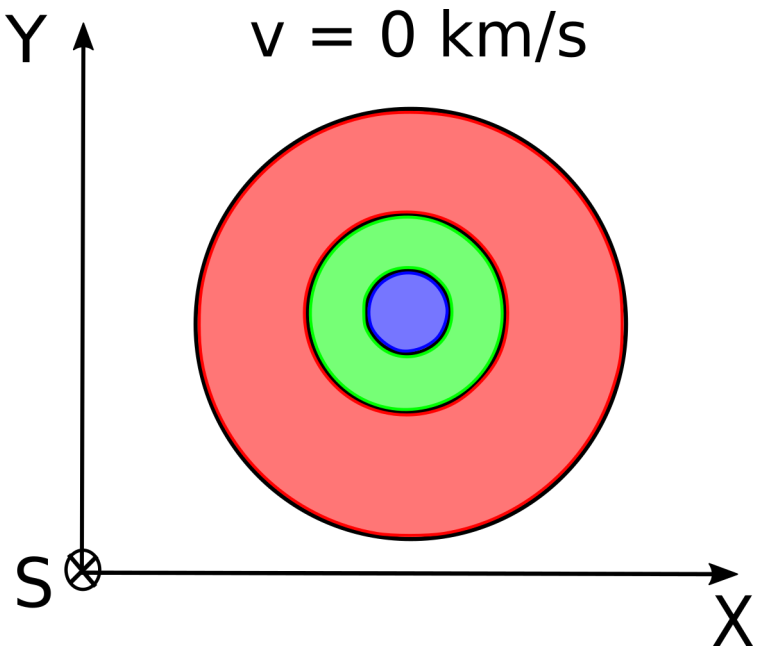

Figure 6.2: A slice in the line-of-sight for a face-on view of the disk at v=0 km/s. Coloured regions roughly denote the same density.

Edge-on view: Next, consider the $i = 90°$ case where the disk is viewed edge-on. Use Figure 6.4 to help visualise and analyse this complex structure. Remember that an X-coordinate represents a slit through the disk along the line-of-sight. All information contained within this slit is then again collapsed onto the line-of-sight axis. A slit at X=0 is depicted in the (y,s)-plane. Such a cross-sectional slit at higher values of X will no longer contain the inner central regions of the disk and therefore will not contain the highest density regions any more. A collapse of such a slit will result in a line at constant X in the (x,s)-plane. Hence, the entire (x,s)-plane represents the collapsing of all X-coordinate slices. It is the velocity field in this plane which needs to be collapsed onto the X-axis to obtain a position-velocity map. The velocity field is at each Y-coordinate alike due to the fully Keplerian assumption. This permits us to depict the velocity field in the (x,s)-plane. The illustration represents contour lines of projected velocity equal to the ones in Figure 6.1. Knowing the volume and density of the moving regions will enable us to comprehend the different amounts of emission.

When probing the disk around $X = 0$ in the (x,s)-plane, both the most rapidly and most slowly rotating regions are encountered. In the PV-diagram, the lowest velocities[2] translate to the center of the PV-diagram and the high-

[2]Remember we talk about absolute values

est ones the outer edges. Collapse-lines at higher values of X no longer probe the highest velocity regions. Therefore, the covered velocity space in the PV-diagrams decreases for increasing X. The lowest velocity regions span a larger X-range wherefore their contribution decreases more slowly than the high velocities, with increasing X-value. This translates itself to the high velocity spikes and the S-shape for lower velocities. Ideally, only the upper right and lower left quadrant of the PV-plot should be filled. As the velocity field is symmetric in absolute value with respect to X=0 but changes sign, the PV-diagram is symmetric with respect to its center. Due to the finite size of the velocity bins and the overall turbulent velocity, both quadrant 'spill' to their adjacent velocity quadrant. This finite velocity width ensures the distinct S-shape.

Because for each X-coordinate, the emitting volume for the lowest velocities is larger than the emitting volume for the higher velocities, the intensity, at each X-coordinate, increases with decreasing velocity. On Figure 6.1, it is clear that the $v = 2$ km/s contour region is largest. This implies that the volume emitting a projected velocity around $v = 2$ km/s is largest and will therefore contribute most to the total flux. It is without doubt not the $v = 0$ km/s region which is largest. The PV-diagram, as well, exhibits a slightly larger flux region in the outer edges of the S-shape. The outer edges of the S-shape decrease again in flux due to low densities in the outer edges and the boundary of our spherical grid whereby the most outer volumes decreases. Note that the former is the dominant term as our grid size is justified by the low densities at its boundary. When looking closely at X=0, one can see that there is a narrow line of less emission in the center of the S-shape. This is due to an optical depth effect. When probing the lowest velocities at $X = 0$, the line-of-sight coincides with (a large fraction of) the emitting column which penetrates part of/the entire disk is a straight line. Therefore, an optical depth $\tau = 1$ is reached more rapidly then for slightly higher values of X, which cut though, as seen on Figure 6.1, the emitting regions.[3]

Inclination: When analysing the effect of the inclination, one can see that, going from $i = 0°$ to $i = 90°$, the narrow slit stretches out to an S-shape with two spikes. As an indication for the battle of largest emitting volumes, the maximum intensity get little by little smeared out from the center to the entire S-shape. Inclining the disk also ensures that no emitting regions are largely parallel to the line of sight, therefore eliminating the narrow strip in the center of the S-shape. The inclination also removes the optical depth

[3]We note that this narrow slit is one pixel wide and the decrease in intensity might have a numerical origin. It is exactly at X=0 which includes the central star in our model. As `LIME` was originally not developed to have a central object of immense intensity, it can be that it has trouble coping with this.

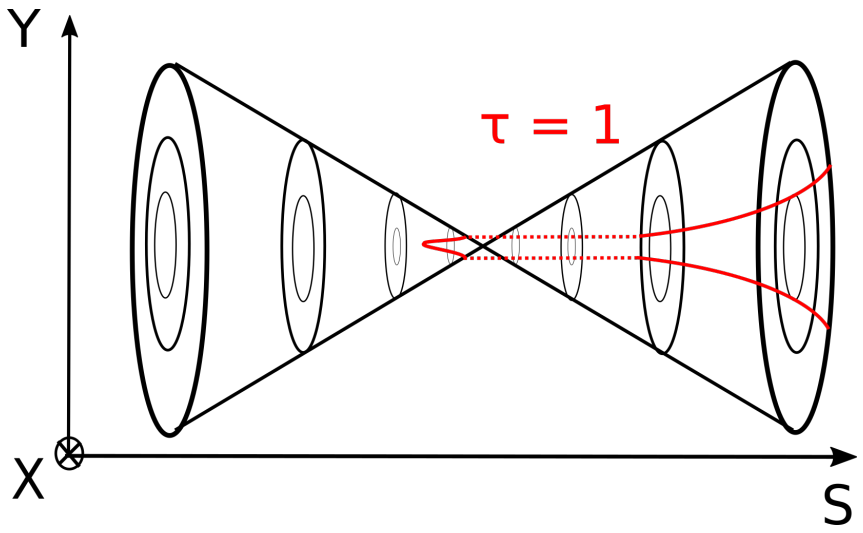

Figure 6.3: X-slice of a face-on view of the disk at $v = 0$ km/s with a possible $\tau = 1$ level.

effect of the $i = 0°$ model as the highest possible density column, the mid-plane, does not get probed entirely anymore.

Collapse onto Y-axis

Face-on view: Let us know consider the collapse onto the Y-axis. Again starting with the face-on view, $i = 0°$. This looks exactly the same as in the previous case, which is trivial as the disk is spatially symmetric when seen face-on.

Edge-on view: The edge-on PV-diagram looks quite different from the previous case, here the disk does not span the entire spatial axis because we cut off the disk at an angle α (see Eq. (4.65)). The maximum value of the Y-coordinate equals H_f. Again Figure 6.4 is extremely helpful to visualize the 3D structure with complex 3D projected velocity field. This time however, a slit is taken in the Y-direction along the line-of-sight. All information in this slit is again collapsed onto the line-of-sight axis. A slit at Y=0 is depicted in the (x,s)-plane. The cross-sectional slices at higher values of Y will be a circular shell as the inner regions of the disk are confined to a limited height. A collapse of all cross-sections onto the line-of-sight-axis is depicted in the (y,s)-plane. As the velocity field is invariant under height, it is easiest to focus on the (x,s)-plane, collapsing this information onto the line-of-sight-axis while keeping in mind, via the (y,x)-plane, which regions are probed at

particular Y-coordinates.

In the (y,s)-plane, one can see that the Y=0 slit probes all regions of the disk. As all regions are probed, all of velocity space is probed as well. Again with the lowest velocities represented by the center of the PV-plot and the highest ones at the edge. When increasing the Y-value, as seen on the (y,s)-plane, the inner disk regions are no longer probed. Therefore, a hole emerges in the center of the (x,s)-plane. Because of this, the highest velocities are no longer probed resulting in a more narrow shape in the PV-plot. As all highest velocities are confined within a small inner region, the loss of high velocity space in the PV-diagram will be quite rapidly. Lower velocities are spread out over a larger radial area whereby their loss in the PV-diagram is more gradually. This gives the PV-diagram its distinct shape, slowly narrowing for increasing Y with two spikes at small Y.

It is obvious that the slit at Y=0 contains the largest volume and has the highest density as it is a slice through the midplane. Increasing in height the emitting volume will decrease, as will the density. Hence, the total flux decreases with increasing values of Y. The PV-plot neatly displays this behaviour. A dip in the $v = 0$ km/s bin with respect to the others is due to the emitting volume being parallel to the line-of-sight, just as for the previous edge-on PV-plot. Here however, it applies to all Y-coordinates as each of Y-slit contains this emitting region. The less emitting narrow line in the center of the PV-diagram is due to the same reason as discussed above. For slightly large values of Y, this effect also comes in to play but as the density is lower, this is less apparent. The combination of these sudden drops in intensity cause the specific colour pattern in the center of the PV-plot.

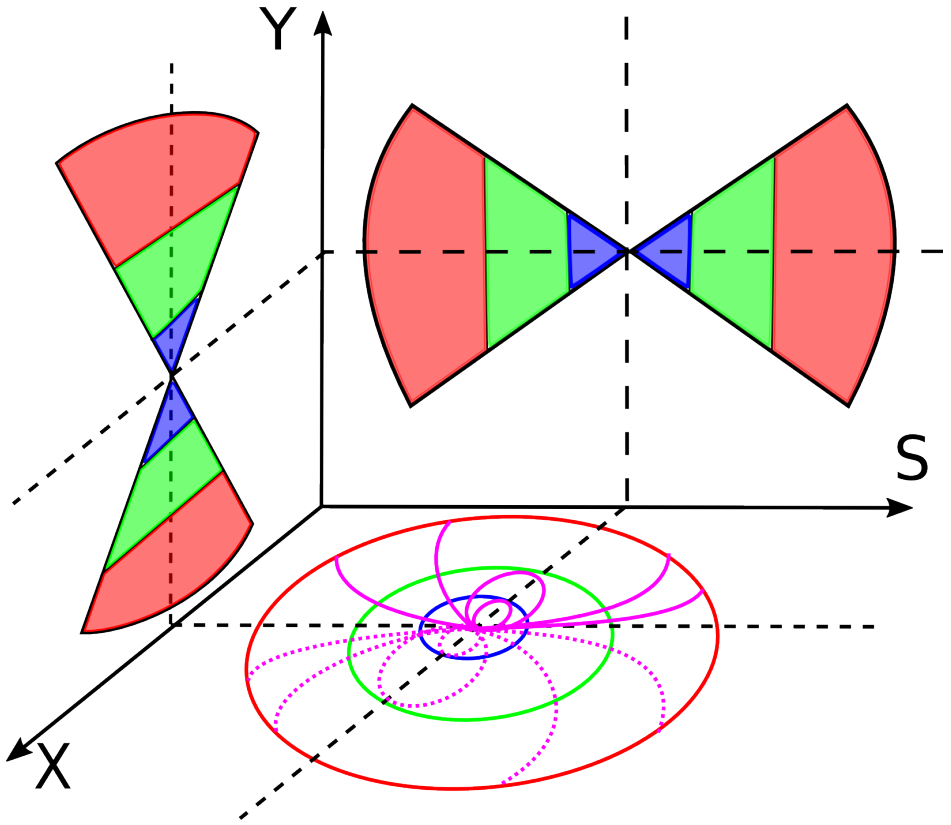

Figure 6.4: Representation of 3D disk viewed edge-on. X- and Y-axis denote horizontal and vertical spatial coordinates respectively. The S-axis follows the line-of-sight. The (x,y)-plane denote a slice at s=0, the (y,s)-plane represents a slice at X=0 and the (x,s)-plane represents a slice at y=0. Coloured areas represent roughly the same density. The projected velocity contours (cfr. Figure 6.1) in the line-of-sight are illustrated in the (x,s)-plane.

Inclination: Inclining the disk from face-on to edge-on will result in a decrease in spatial coverage of the disk and an increase in projected velocity. This is visible in the evolution of the PV-diagrams as the narrow slit is contracted in the Y-range and stretched in the velocity space. During this inclination, two new optical depth effects arise. One is most clearly visible at $i = 36°$, where a hole of less emission is created. To simplify the analysis, consider viewing the disk at $v = 0$ km/s. The contour line $v = 0$ km/s in Figure 6.1 denotes the emitting region. This region does not change when inclining the disk. Figure 6.5 shows the line-of-sight of the Y-value which denotes the most upper point of the inner edge, for different inclination angles. All Y-values below this limit probe much smaller volume as they cut off part of the disk, resulting in a lack of emission. The higher the inclination, the higher this Y-limit, the larger the gap in the PV-diagram. This gap disap-

pears at an inclination α, which denotes the disk/wind interface. From this inclination onwards, the line-of-sight always needs to probe the entire length of the disk. This reasoning was done for $v = 0$ km/s but holds as well for the slightly larger values with the difference being the size of the gap, as can be seen in the PV-plots.

The second opacity effect can be seen most clearly for inclinations $i = 36°$ and $i = 54°$. Here, the upper part of the PV plot shows more emission than the lower part. Following both lines-of-sight at an inclination $i = 36°$ on Figure 6.5, one notices that the upper line first encounters a higher density than the lower line does. The upper line therefore will reach an optical thick regime more rapidly than the lower one, resulting in less emission in the upper part. This effect is enhanced because the upper line goes from a small emitting region to a larger one. The lower line already probes larger emitting volumes first. This reasoning holds for all inclination angles between the face- and edge-on, and applies to the entire velocity field.

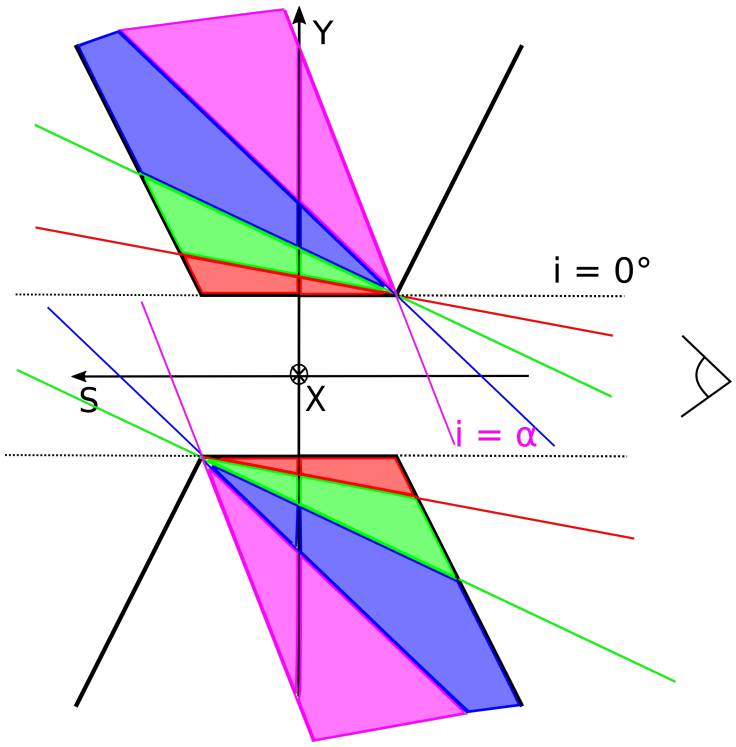

Figure 6.5: The coloured lines represent the lines-of-sight at different inclination angles through the region of the disk that is emitting with projected velocity $v = 0$ km/s. Starting from $i = 0°$ (black) to $i = \alpha$ (pink). The coloured areas viusally denote the area under the line. Note that this is a zoom in on the inner region of the disk.

6.1.2 Bipolar WIND model

Now let us turn to the less complex bipolar wind. Following the same procedure as for the disk, we first take a look at the collapsed data cube onto the X-axis.

Collapse onto the X-axis

When viewing a spherical wind, the whole velocity space has to be covered as the total velocity vector goes from completely away from us to perpendicular to the line-of-sight upto coming completely towards us. By this means, the projected velocity takes all values between both extremes. Here however, a disk obstructs part of the wind, which will erase part of the spherical wind PV-diagram. Note that we will not model a spherical wind but a bipolar one, still satisfying the geometrical separation, as we are interested in the impact of the latter on the PV-plots and line profiles.

Face-on view: When viewing our bipolar wind face-on ($i = 0°$), the disk ensures that the spherical part with lower projected velocities is not reached by our bipolar model. This gap in velocity space is clearly visible in the PV-diagram. Figure 6.6 will help visualize these complex projections. The (x,y)-plane represents a projection of the whole wind in the line-of-sight. The (y,s)-plane depicts a slit at constant value X=0, whereas the (x,s)-plane display a slit at Y=0. As the velocity field in not invariant to any coordinate, it is illustrated on both cross-sections. To produce the velocity plot for the X-axis collapse, all information of an X-coordinate slit needs to be projected onto the line-of-sight-axis.

Looking at the X=0 slit, via the (y,s)-plane, one can see that all possible velocities are probed. This is also clear when viewing the PV-diagram. Going to higher values of X, note that the cross-sectional slit no longer looks like a double cone, but rather to a double cone without the inner part. Following a line of constant X in the (x,s)-plane can help visualize this. At this value, the inner column of the cone is no longer probed whereby the largest velocities are no longer visible. This increasing lack of higher velocities for increasing X-values, translates itself into the distinct slopes in the PV-diagram.

As a slice through X=0 encloses the largest possible volume, the maximal emission is located here and decreases with increasing X. Each velocity is emitted from a conical shell and as we have a spherical grid, the volume of each of these shells is equal which should result in an evenly distributed flux over velocity space. However the highest velocities contribute less as they arise from higher density regions for which optical thickness is reached more rapidly. This increase in flux towards lower velocities declines again

at a certain velocity, this turning point is represented by the red dot in the PV-diagram. This is due to the constant battle between optical thickness and the density. Note that for high optical depths still some percentage of the photons escape which for strongly emitting high density regions can still contribute significantly.

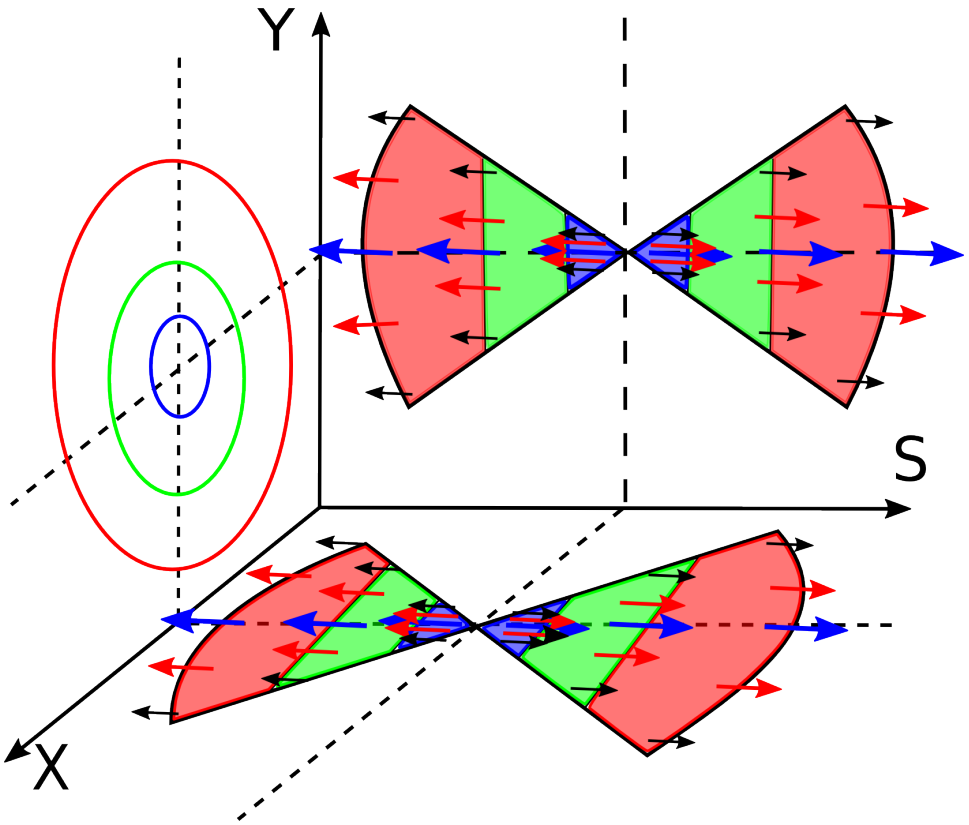

Figure 6.6: Representation of the 3D wind viewed face-on. X- and Y-axis denote horizontal and vertical spatial coordinates respectively. The S-axis follows the line-of-sight. The (x,y)-plane denotes a slice at constant s-coordinate, the (y,s)-plane represents a slice at X=0 and the (x,s)-plane represents a slice at y=0. Projected velocity, in the line-of-sight, is illustrated with coloured arrows, where each colour represents the same magnitude.

Edge-on view: Next, consider the PV-diagram when the wind is seen edge-on. Figure 6.7 will be quite useful interpreting this plot. The (y,s)-plane depicts a slice at X=0 through the cone. The (x,s)-plane on the other hand, represents a cross-section at constant Y where the concentric circles denote the conical shells. Note that these circles reduce in size for decreasing values

of Y, but still preserve the conical shell shape.
Looking at the X=0 slices, one can see in the (y,s)-plane that all possible velocities are probed. Cross-sections of increasing X, again, no longer contain the inner parts of the cone, as can also be seen in the (x,y)-plane. Examining the (x,s)-plane learns us that at these higher X-coordinates the highest velocities are no longer probed. This decrease in velocity space for increasing X, expresses itself in the slopes in the PV-diagram resulting in the almost circular shape.

As for each X-slice, all velocity emitting volumes are equal in size, the flux distribution should again be evenly distributed over velocity space. However, as the density increases inwards the lower velocity regions will contribute more as this is where they are situated. Yet, increasing density will permit the optical thick regime to be encounter more rapidly. This balance gets tipped over in favour of the optical depth as some turning velocity, which for the X=0 slices is denotes by the most red dot. From this point onward, the emission will decrease again. This effect is less apparent at higher X-coordinates as there, the densities are lower and this optical depth effect might not even be in play. One can also see that there is a trace of blue wing absorption which arises as the cold, low density regions are probed first for the negative velocity whereas for positive velocity, a hotter and more dense region is encountered before reaching an optical thick regime. It is the temperature and source function which are responsible for this effect.

Inclination: Inclining the conical wind will allow for the presence of lower projected velocities. When it has been tipped over by more than the inner angle of the cone α, the highest projected velocity will no longer be seen. This is clearly visible in the PV-diagram, the outer edges start from $v = 15$ km/s for $i = 0°$ and decline to about $v = 10$ km/s for $i = 90°$. The battle between optical depth and density is most clearly visible around X=0 and depends on what density regions a line-of-sight penetrates, which of course depends on the orientation of the wind. The blue wing absorption also decreases with higher inclination which depends on the first encountered density regions of the line-of-sight for opposite velocities, which obviously changes with inclination.

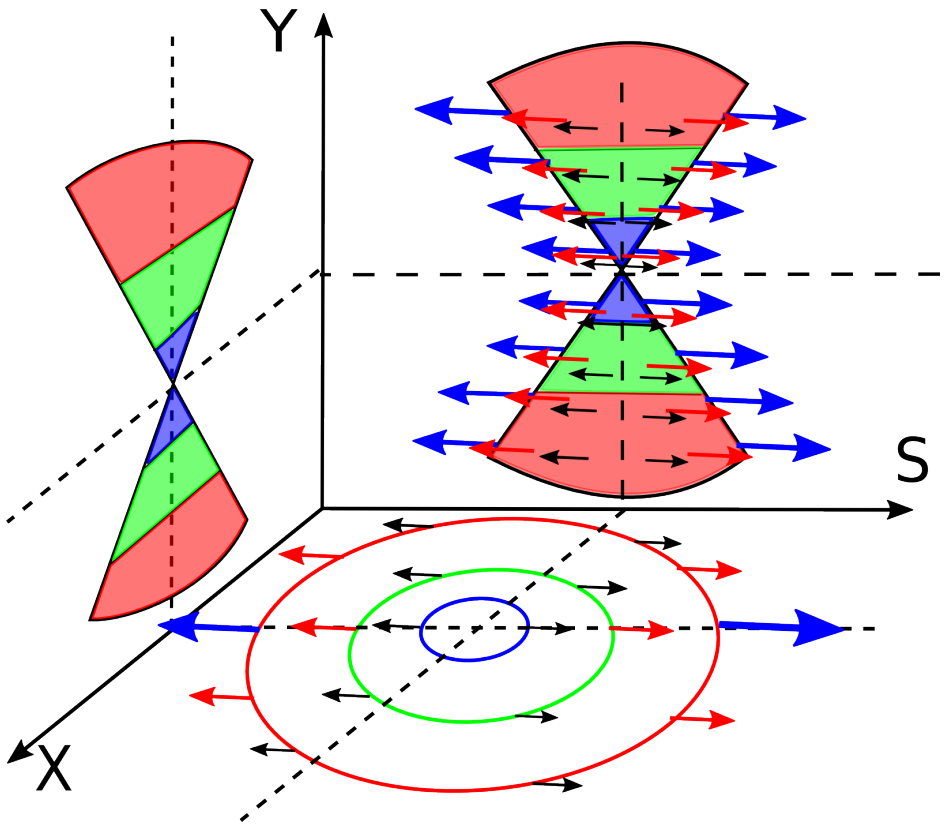

Figure 6.7: Representation of the 3D wind viewed edge-on. X- and Y-axis denote horizontal and vertical spatial coordinates respectively. The S-axis follows the line-of-sight. The (x,y)-plane denote a slice at constant s=0, the (y,s)-plane represents a slice at x=0 and the (x,s)-plane represents a slice at constant y. Projected velocity, in the line-of-sight, is illustrated with coloured arrows, where each colour represents the same magnitude.

Collapse onto Y-axis

Face-on view: Let us now turn to the collapse of the data cube onto the Y-axis. Due to the symmetry of the cone, the face-on view is exactly the same as for the X-collapse.

Edge-on view: The edge-on view, on the other hand, looks quite different. Figure 6.7 will again be of great use for the comprehension of the yielded data. As stated before the (x,s)-plane is a slit at constant Y. This circular size decreases for decreasing Y, as seen on the (y,s)-plane, but the velocity fields stay identical. To render the PV-plots, all information on such a slice needs to be collapsed onto the line-of-sight-axis.

Consider a slit at Y=0, according to the (y,s)-plane only a tiny part of the cone in probed but it is too small to be discernible on the PV-diagram. This also holds for slightly larger Y-values, hereby a narrow blue line is present in the PV-diagram. Increasing the Y-coordinate, the probed volume becomes significant and as shown in the (x,s)-plane, all possible velocities are encountered. When reaching the Y-value where the upper spherical part of the cone starts, the highest velocities will no longer be probed when increasing the Y-coordinate. The former results in a rectangular shape whereas the latter produces the rounded shape in the PV-diagram.

The intensity increases with increasing Y because the radius of the circular slit increases resulting in a larger emitting volume hence a more extensive flux contribution. Reaching the spherical part of the cone, the cross-section decreases again resulting in less emission. The emission for large velocity values is less because, as seen on the (x,s)-plane, the highest velocities only arise from the outer regions whereas the lower ones emerge from the regions throughout the whole cone, giving the latter a larger emitting volume which leads to a higher flux in the PV-diagram.

Inclination Inclining the bipolar wind, is like inclining a double cone, which is exactly what you see on the PV-diagrams. From a cone lying down, for $i = 0°$ to one standing up when $i = 90°$ is reached. The red parts denote the interplay between high optical depth and high density emission.

6.1.3 REF model

PV-diagrams

After a thorough interpretation of both wind and disk PV-diagrams, we now can combine them to understand the PV-diagram of the reference case (REF). Here, one can see that the disk is the dominant contributor of flux. The dominance of disk and wind will vary depending on the parameter combination. One just has to give a different weight to the contribution of WIND or DISK model in order to lift the degeneracy in the combined models. This is the strength and whole purpose of the DISK and WIND model. You only have to keep in mind, that when disk en wind overlap in the line-of-sight, optical depth effects might come into play which were not present in either one of the separate models. Therefore it is not just adding up two PV-plots.

Line profiles

PV-diagrams are not the only way to analyse a complex outflow structure. Line profiles provide an excellent overview of the global velocity structure. These give an insight on how much material is being propelled and at which

velocities. The line profiles of the reference model are shown in Figure 6.9. Once again, it is easiest to first consider both DISK and WIND models to get a notion of what their impact is on the global line profile.

Let us start with the disk model which has a peak around $v = 0$ km/s when seen face-on. This is exactly what we expect from previous discussion in section 6.1.1 . When inclining the disk, the area under the peak gets distributed over larger velocities. This central peak reaches its lowest amplitude when the disk is seen edge-on. A small dip in the top of the bulge at $i = 90°$ can be seen mainly due to the optical depth effect of the edge-on disk when projected onto the Y-axis.
When looking face-on, the WIND model shows two distinct peaks with a gap in velocity space. This gap, as discussed above, arises as the disk prohibits these low projected velocities to be reached. When inclining the wind, the area under both peaks is spread out to lower velocities. Between $i = 36°$ and $i = 54°$ a turning point has been reached where the inner velocities become the more dominant contributors. The exact turning point is at an inclination $i_{tp} = \alpha$, which denotes the inner angle of the bi-conical wind. As discussed above, from this point onwards, the maximum projected velocity will decrease as can be seen when looking at the velocity range in the edge-on profiles.
Combining both models results in the REF model. For this average parameter combination, the wind contributes less to the total emission. The contrast between wind and disk emission, however, will decrease for increasing inclination angle.

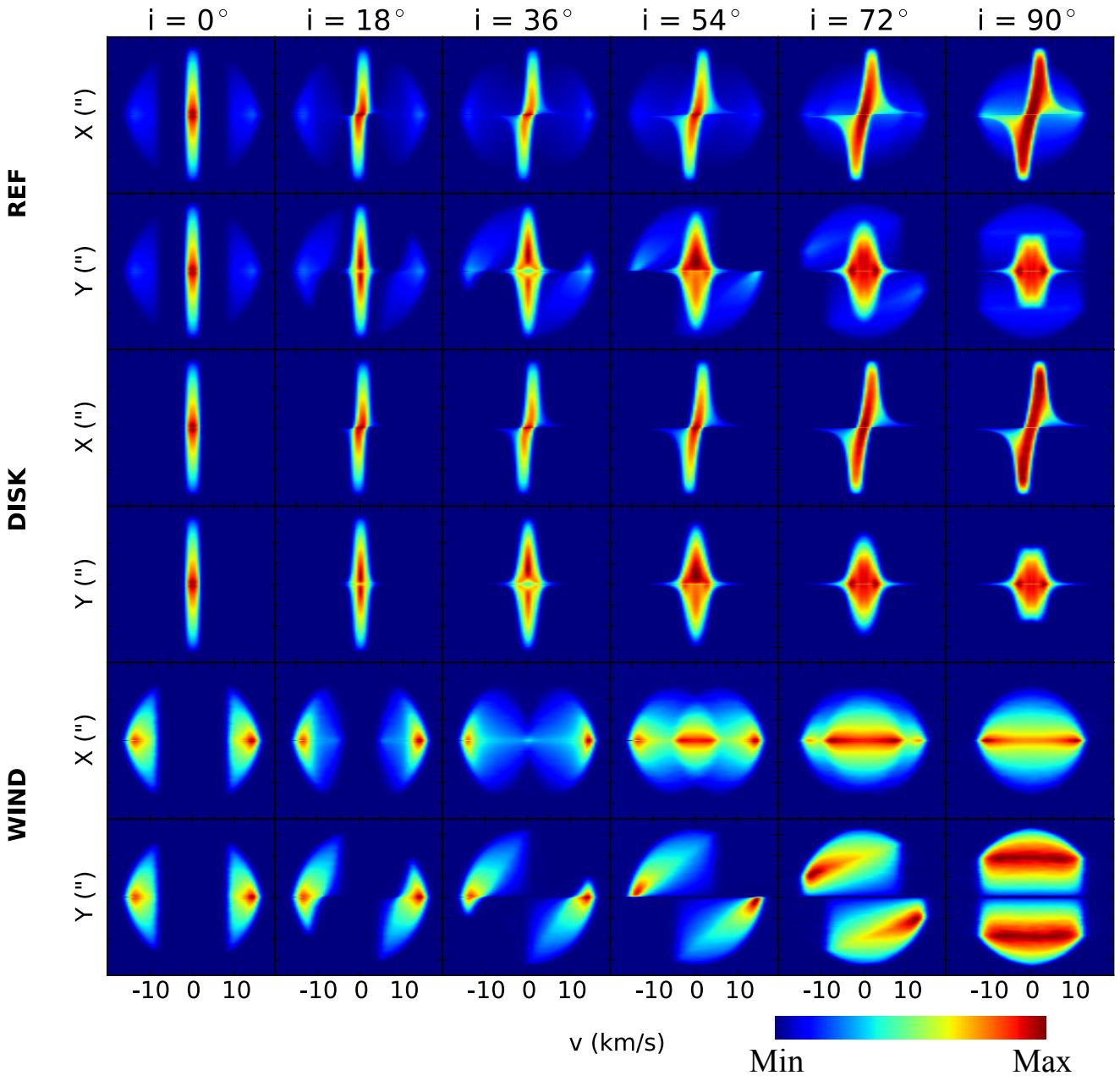

Figure 6.8: The PV-diagrams of the models REF, DISK and WIND, each spanned over two rows. The top row of each model represents a collapse of the 3D data cube onto the X-axis. The bottom row of each model represents the collapse of this data cube onto Y-axis. Each column presents an image of the PV-diagram at a different inclination angle. The colours represent the amount of flux with red the maximum amount and blue the least. It is important to note that none of the PV-diagrams are on the same scale. The bottom axis represents projected velocity space. Each model takes parameter values according to Tabel 5.2.

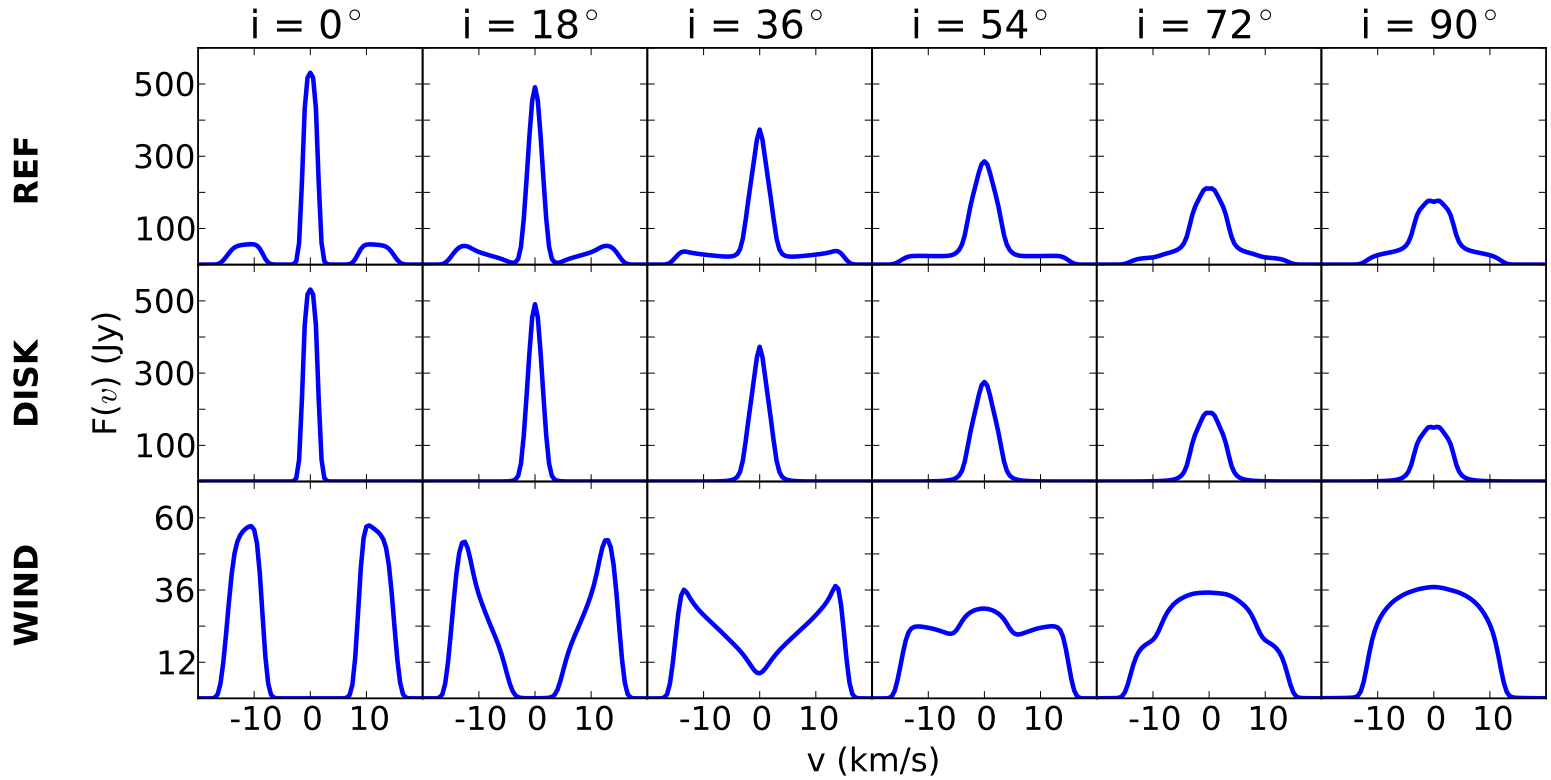

Figure 6.9: Line profiles for the models REF, DISK and WIND with their parameter combination given in Tabel 5.2. Each column represents an inclination angle by which the structure is oriented. The line profiles denote the amount of flux in Jansky as a function of velocity in the line-of-sight.

6.2 Mass loss rate

The range in mass loss rate for AGB-stars is quite broad, as mentioned above the star can lose $10^{-8} M_{\odot}$/yr up to $10^{-4} M_{\odot}$/yr. This range of several orders of magnitude will definitely impact the radiative transfer through the bipolar wind. We therefore need to examine the impact of a change in mass loss rate in the radiative output and how we can observe this. It might be that the changes in PV-diagram are non-significant but the line profiles show some clear distinction. It can be as well that some dramatic optical depth features become apparent. As stated above, we will only change the mass loss rate parameter in the REF model to inspect its impact. The PV-diagrams of the models high mass loss (ML5), the reference case (ML6) and low mass lose (ML7) are displayed in Figure 6.10 with parameters given in Tabel 5.2. To simplify the comparison with the reference model, ML6=REF is depicted in the central part of the figure.

PV-diagrams: Let us start with the lower mass loss rate ML7. This low mass loss rate supplies less material to the conical shape, resulting in less emission. The contrast between high and low emission contributions of this wind on the PV-plot, as is clear in the WIND model, are slightly to non-visible. This limited visibility will definitely not be distinguishable from observations. Optical depth effects are not visible either, this due to the slim emission contrast but also, as the density is lower, these effects are less profound.
The high mass loss model ML5 on the other hand, shows a large impact on the PV-plots. When the wind and disk emission regions in the PV-diagram overlap, which is most clearly at $i = 90°$, the strong wind emission alters the disk emission part. For the X-collapse, the small emission region of the inner part of the cone (around X=0) will now have a high enough density to contribute to the disk emission in this region. Therefore the two horizontal spikes broader, as compared to the ML6 model. The rectangular shape of the wind-PV is significant enough to alter the global view of the PV-diagram. For the edge-on Y-collapse PV-plot, the central region gets blown up, eliminating the nicely delimited spikes visible in the ML6 model. The highest flux regions are no longer in the outer parts of the S-shape but are in the inner part as the wind contributes a lot to the center but only a little to the edges, as can also be seen in the WIND model. These extra wind contributions have shifted the high emission regions in the for PV-plots where both wind and disk overlap. Optical depth effects are stronger and therefore also more clearly visible. The blue wing absorption when seen face-on is quite noticeable.

Line profiles: The line profiles are displayed in Figure 6.11. When comparing the three models for the face-on case, it is clearly visible that the

bulges, due to the wind, are more apparent for the high mass loss than for the loss mass loss rate, which is of course what we would have expected. You may also notice that the bulges are sharper for high mass loss and flatter for the ML6 model. This sharpening is due to the optical depth effect, which is more profound for higher mass loss. If the lowest mass loss rate bulges would have been more clearly visible, we would expect these ones to be the most flat, as the optical depth effects are minimal or even non-existent.
Looking at the edge-on case, we can clearly see that the higher mass loss rate will give rise to a larger overall intensity as the wind emission gets more important. As expected, the weak wind will be almost indistinguishable from a pure disk model. Notice that for the strong wind, a clear dip in the top of the bulge arises. This is an enhancement of the optical depth effect already present, as discussed above, in the disk around $v = 0$ km/s. As the lines-of-sight not only penetrate the disk but also the wind, the optical depth effect increases the contrast between optical thin and thick velocity-region. This contrast increases with increasing density, hence increasing mass loss rate.

As always, increasing inclination lowers the highest amplitude peak by spreading its area over higher velocities. The velocity gap, for $i = 0°$ gets filled as well, reaches a plateau for $i = \alpha$ and keeps increasing onwards.

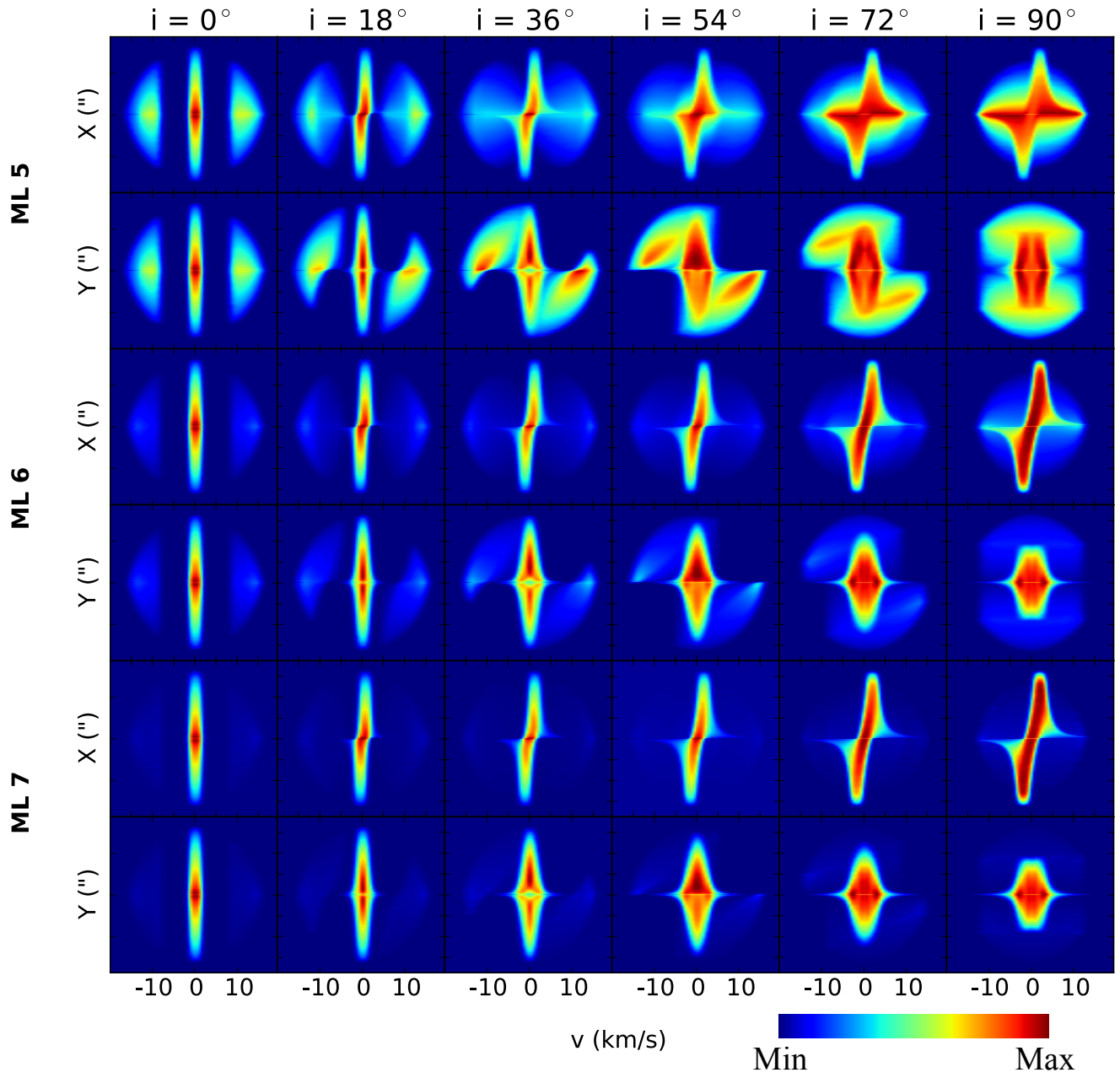

Figure 6.10: The PV-diagrams of the models ML5, ML6 and ML7, each spanned over two rows. The top row of each model represents a collapse of the 3D data cube onto the X-axis. The bottom row of each model represents the collapse of this data cube onto Y-axis. Each column presents an image of the PV-diagram at a different inclination angle. The colours represent the amount of flux with red the maximum amount and blue the least. It is important to note that none of the PV-diagrams are on the same scale. The bottom axis represents projected velocity space. Each model takes parameter values according to Tabel 5.2. This grid of models shows the impact of the mass loss rate on the PV-diagram.

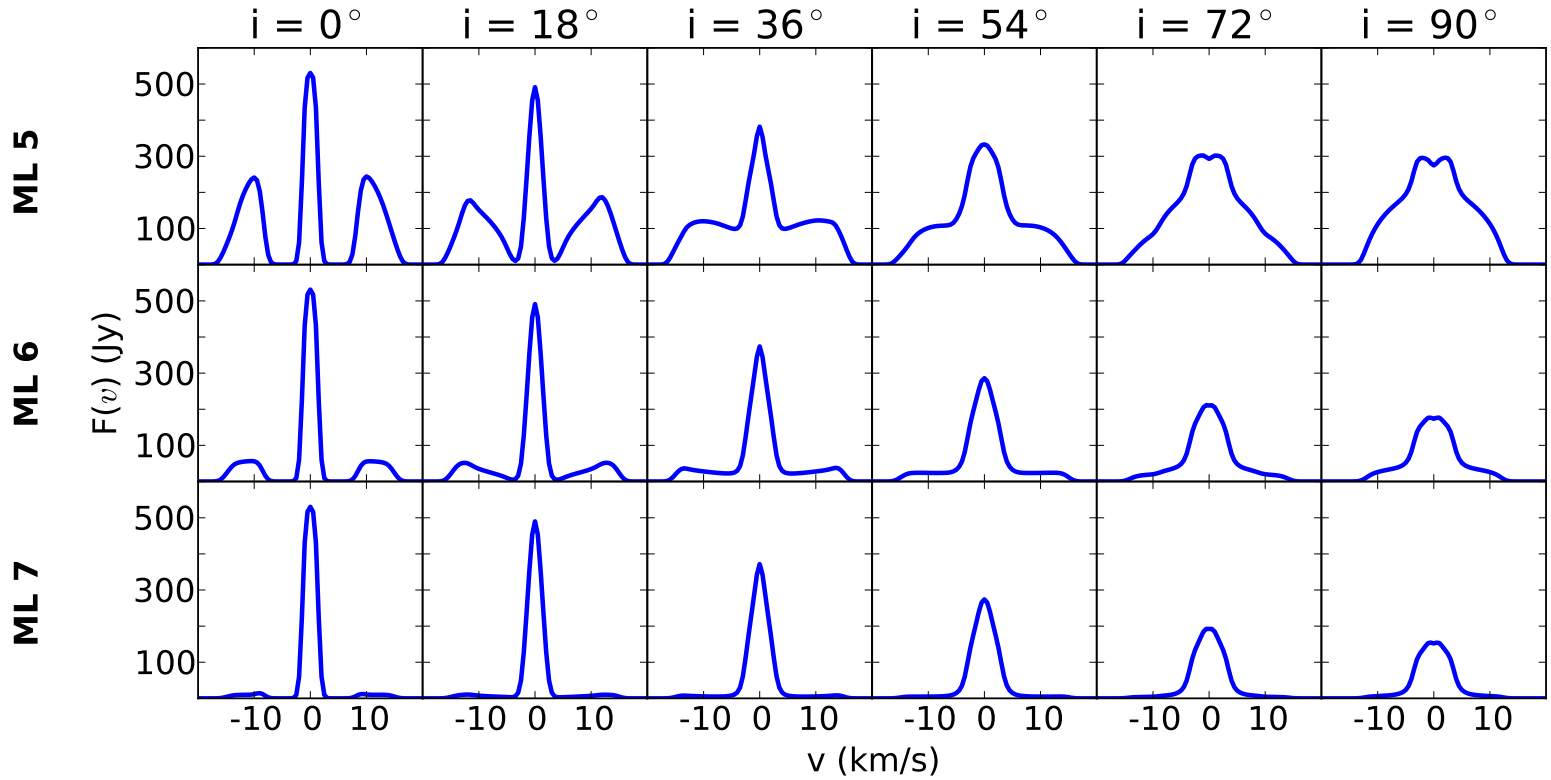

Figure 6.11: Line profiles for the models ML5, ML6 and ML7 with their parameter combination given in Tabel 5.2. Each column represents an inclination angle by which the structure is oriented. The line profiles denote the amount of flux in Jansky as a function of velocity in the line-of-sight.

6.3 Disk mass

The range in disk mass can be several orders but as discussed above we will limit ourselves to a range between $M_{disk} = 0.1 M_{\odot}$ and $M_{disk} = 1.0 \cdot 10^{-5} M_{\odot}$. A difference of orders of magnitude will definitely impact the radiative transfer through the disk. We would expect that the intensity of the more heavy disk will be higher than for the small disk as it has much more material that emits. Optical depth effects will probably be more important as well. The PV-diagrams and line profiles are depicted in Figures 6.12 and 6.13 respectively.

PV-diagrams For the low mass disk we expect the same result as for the ML5 model discussed earlier because it is the contrast/ratio between disk and wind which is most important for the global view of the PV-diagram. The only difference here is the wind being more dominant than the disk. Optical effects will obviously be different as well. When comparing the ML5 model with the MD5 model, we do notice that the global view of the PV-plots look similar. Just the disk contribution parts are less intense what puts the most intense emission parts, red in the plot, in the wind sections. The optical depth effect which gives rise to an increase in emission in the upper disk part for inclined disks models is no longer visible. The creation of the gap for inclination between $i = 0°$ and $i = \alpha$, on the other hand, is still visible. Both effects are discussed in the paragraph 'Inclination' for Y-collapse PVs of the DISK model section. The optical depth effect which reduces the intensity around $v = 0$ km/s for the edge-on Y-collapse PV is even more apparent.

Due to computational issues, we are not able to infer information from the heavy disk output. For some reason, `LIME` has difficulty distinguishing wind from disk when appointing the grid cells.
However, we only expect the disk emission areas in the PV-plots to be more intense with an increase in optical depth effects.

Line profiles: As expected the line profiles for the low mass disk resemble the strong wind ML5 model. The only difference being the scale of the intensity. Due to this intensity with respect to most models, small differences are more apparent in the line profiles. As the spectral signatures of the heavy disk are not usable, we cannot compare both extremes. As always, the impact of the inclination is severe.

Figure 6.12: The PV-diagrams of the models MD5, MD3 and MD1, each spanned over two rows. The top row of each model represents a collapse of the 3D data cube onto the X-axis. The bottom row of each model represents the collapse of this data cube onto Y-axis. Each column presents an image of the PV-diagram at a different inclination angle. The colours represent the amount of flux with red the maximum amount and blue the least. It is important to note that none of the PV-diagrams are on the same scale. The bottom axis represents projected velocity space. Each model takes parameter values according to Tabel 5.2. This grid of models shows the impact of the disk mass on the PV-diagram.

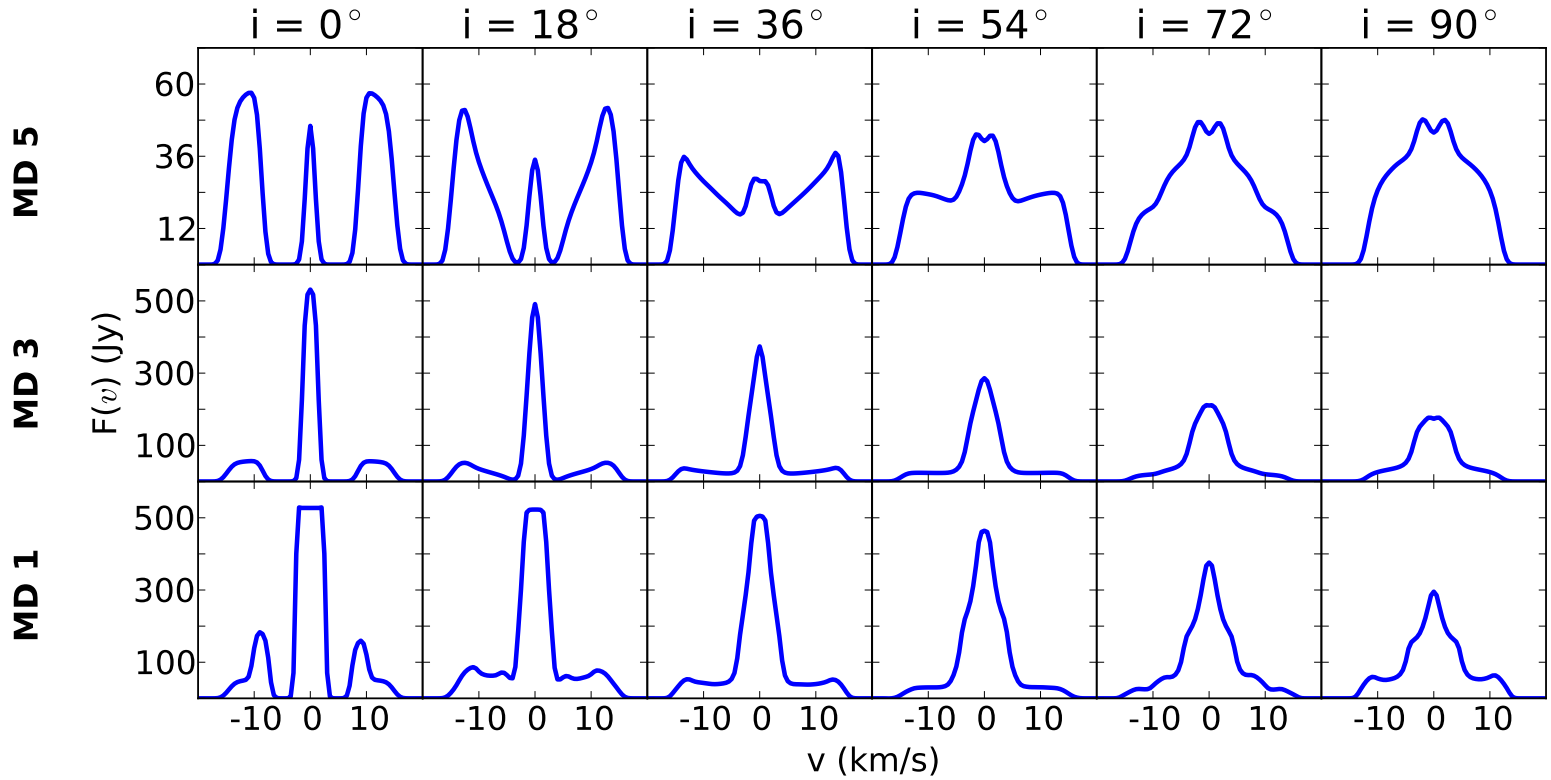

Figure 6.13: Line profiles for the models MD5, MD3 and MD1 with their parameter combination given in Tabel 5.2. Each column represents an inclination angle by which the structure is oriented. The line profiles denote the amount of flux in Jansky as a function of velocity in the line-of-sight.

6.4 Keplerian velocity zone

Our assumption of a fully Keplerian disk is, as discussed before, probably not the most realistic one. We therefore introduced a transition zone between disk and wind which lets the wind penetrate the disk radially and gradually decrease in magnitude. How fast this decline in magnitude really is and when it vanished, depends on the parameter k and the angle ζ, where this latter is determined by stating what fraction of the disk only rotates Keplerian. In reality this fraction and steepness of decline will probably depend on both wind and disk properties. A strong wind will penetrate the disk more deeply. A heavy, dense disk will let the wind only penetrate its surface. We, however, do not take in account these effects. We will only probe the effect of the extent of this transition zone on the PV-diagrams and line profiles for our reference case. Intuitively, we believe that an intermediate zone of no more than twenty percent is the most realistic one. As a toy model, we will also probe a disk which is only 50% Keplerian and one for which the wind has penetrated it completely. The PV-plots for all five different models, with their respective parameter combination given in Tabel 5.2, are presented in Figure 6.16. Because the velocity profile is to complicated we can no longer use illustrative representations, hence we need to rely on computed contour plots. Due to its 3D complexity, no easy projections are helpful. Therefore, we provide four X and Y slices through the disk which will enable us to compose a rough view of the velocity field. They will also provide the necessary information to reproduce the PV-diagrams. As the smallest transition zone models do not show large dissimilarities, we will first analyse the more extreme models.

KVZ50 model: Let us start to discuss the KVZ50 model. Consider the X-collapsed data cube for an edge-on view of the disk. X-and Y-slice projected velocity contour plots are shown in Figure 6.14 respectively, at coordinate values depicted in the figures. For this PV-diagram, the X-slices are useful to take a look at. Similar to the 3D representations, all information on these plots needs to be collapsed onto the line-of-sight. The inner Keplerian parts ensures the double spiked S-shape. At X=0, one can see that the full velocity space is run through. For increasing values of X, the highest projected velocities are no longer present, hence the two slopes in the PV-diagram. One side of velocity space declines less rapidly than the other, depending on which side of the disk is probed. This is because the radial wind is counteracting the disk rotation on one side and aiding it for the opposite rotation part. From the X=10 AU slice, one can see that the most extreme velocities make up a significantly large section of the disk. This translates itself in the two high intensity dots in the PV-diagram. Increasing the X-coordinate evens out all emitting volumes to roughly equal size, resulting in a uniform increase of

flux throughout the PV-plot. Do not forget that the bipolar wind intensity contribution is also contained in this plot but as the wind is not altered by this transition zone this does not change.

Next, consider the Y-collapse for a disk seen edge-on. The distinct shape of a bipolar wind is still conserved. The disk contribution, however, loses its top and bottom as these mainly arise from large emitting volumes at high Y-values. This region is now replaced with a transition zone, redistributing the emission from the lost top and bottom part. Figure 6.14 tells us that for all Y, the entire velocity space is covered. The spherical part of the wind, which is at the edges of the Y-axis, does not contain a transition zone and hence is not affected. At high Y, it is clear from Figure 6.14 that the highest velocity regions are largest, therefore they contribute most to the total emission. When decreasing in Y, the maximum intensity contribution gets evened out towards lower velocities, as volumes become roughly equal in size. While decreasing in Y, the Keplerian velocities become more dominant than the transition zone contributions as this latter zone reduces in size.
Note that no additional optical effects come into play as the transition zone consists of a lot of narrow velocity regions, thence it is not able to reach a high optical thick regime.

KVZ0 model: Let us now consider the KVZ0 model where we will first take a look at the X-collapse PV-plots. For $i = 90°$ the PV-plot does, at first sight, not look anything like the ones before, the S-shape is completely obliterated. Note however that by tuning the colour range of the intensity maps, this might not be the case. At X=0 we see that all of velocity space is probed. Just like in the previous situation, this range diminishes asymmetrically for increasing X. Let us take a look at the X-slices of this velocity field, displayed in Figure 6.15. On all slices, around Y=0 there is still some little part which rotates Keplerian. This is because the radial contribution has almost no contribution at the midplane of the disk as here the smoothing function drops to zero. Therefore, we can still see a faint S-shape in the PV-diagram. As can be seen on the slice at X=0, the highest velocities have the largest areas, hence highest flux on the PV-plot. The PV-diagram also shows signs of blue wing absorption for these high emission regions. This is because these emitting regions cover the whole length of the disk and are large enough to notice this optical depth effect. This holds for X-coordinates close to X=0.
The Y-slices in Figure 6.15 provide a tool to comprehend the Y-collapse PV-diagram. Again at the outer edges in Y-space, the higher velocity zones are a bit large. When decreasing in Y, the lower ones become larger and therefore more dominant. As the radial contribution has dropped almost to zero around the midplane, no large high velocity regions are present here. This

shift in maximum emission is represented by the curves in the PV-plot. As all volumes are quite small, the density is an important factor for the total emission. As this is highest in the midplane, this region will contribute more, as can be seen in the PV-plot.

General: The impact of the transition zone for a face-on view is straightforward. Look at it as an extension of the wind. When seen face on, the edges of the wind-cone provide the lower projected velocities. As the cone extends, lower projected velocities are reached. A decreasing Keplerian fraction model will have an increasing transition zone whereby the gap of low velocities gets little by little filled. This is exactly what we see going from top to bottom for $i = 0°$ in Figure 6.16. For large transition zones, the intensity of this velocity gap exceeds that of the wind contribution as the transition zone keeps the density profile of the disk, which is higher than that of the wind.

The effect of the inclination is somewhat difficult to analyse profoundly. In general, the transition zone takes over part of the disk and smears this intensity out over all of velocity space. Optical effects on the disk will decrease as well due to less disk-velocity material

Line profiles: The decrease in disk-flux with increasing transition zone can also be seen in the line profiles, presented in Figure 6.17. By following a column at each inclination, we can see that the central peak decreases in amplitude. For $i = 0°$ the 'lost' disk emission redistributes itself by the visually filling of the velocity gap. For the extreme cases this region is even more dominant than the highest velocities. The peak at $v = 0$ km/s did not vanish as due to the decrease in magnitude, with deeper penetration, the region around the midplane still rotates nearly Keplerian. As this is the most dense region, it radiates most strongly.
As discussed above, for the edge-on view the original disk emission gets spread out over all of velocity space. This translates itself in the line profile as a decrease of the central peak with its area spread out over all velocities, flattening the whole line with increasing transition zone.
Inclining the object has the same effect as always, contributing to the low velocities and decreasing the central peak.

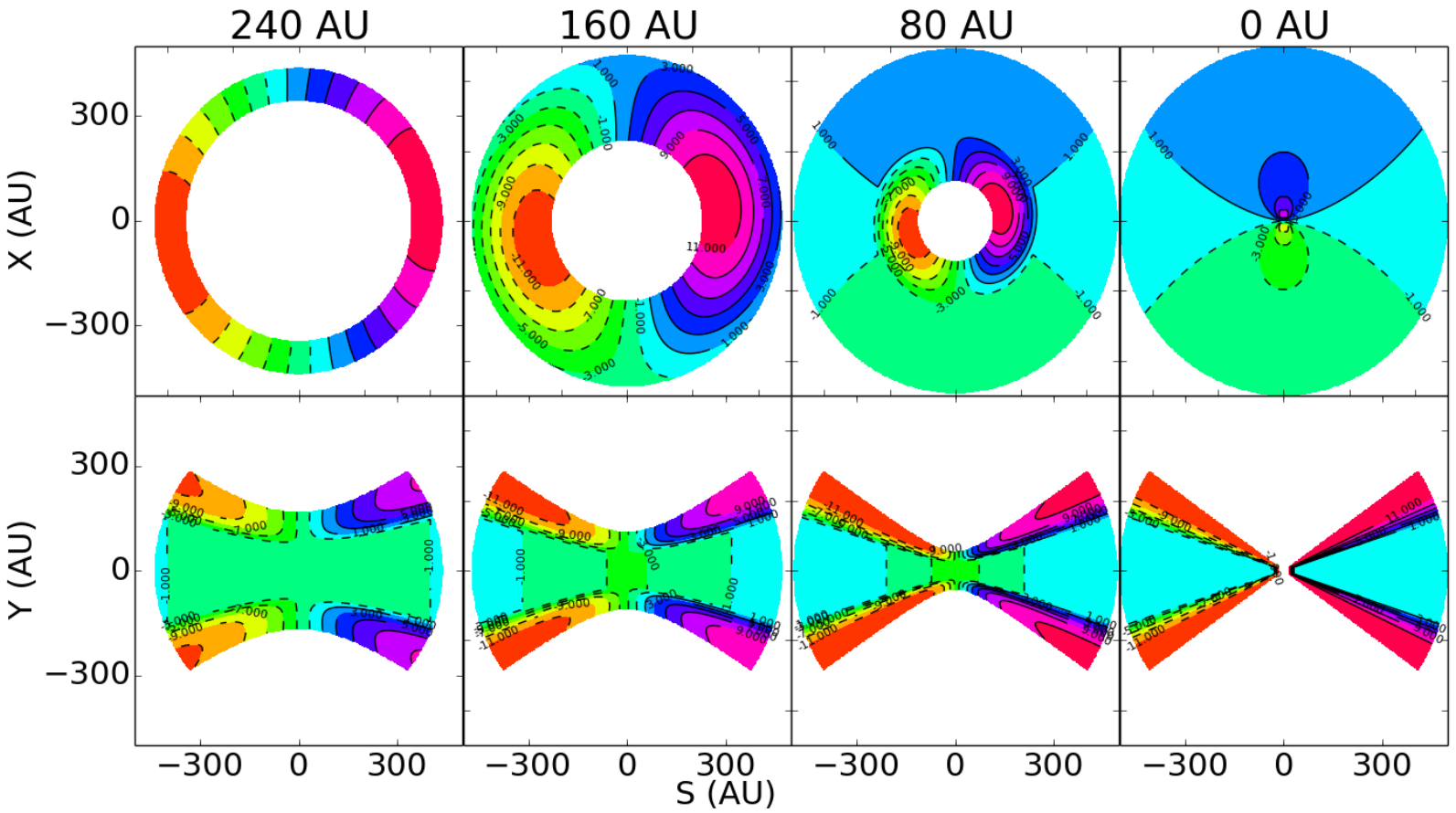

Figure 6.14: X- and Y- slices through the disk at Y- and X-coordinates of 240, 160, 80, 0 AU, respectively for the model KVZ50. Colour regions denote the equal projected velocity in the line-of-sight (S-axis).

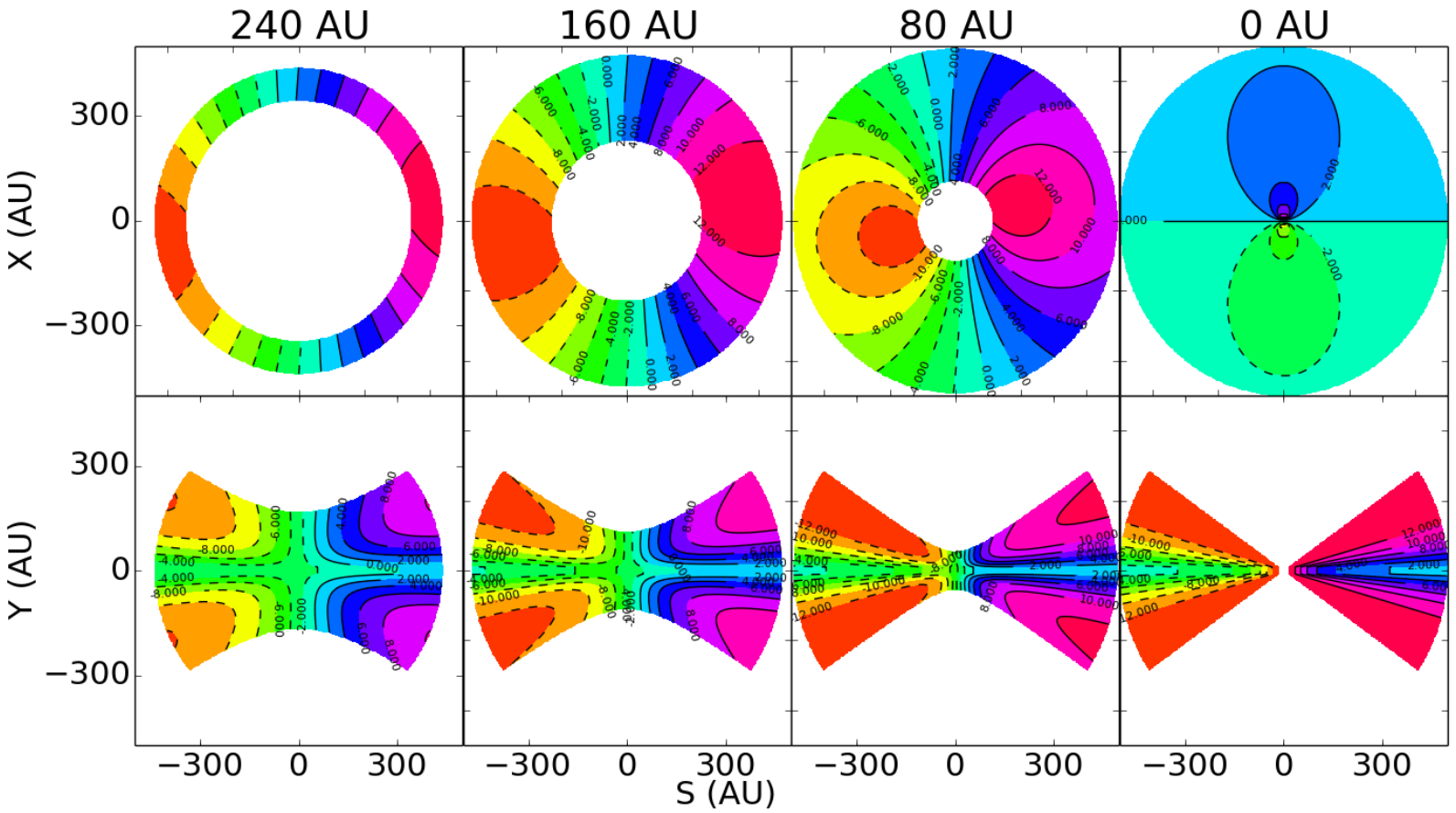

Figure 6.15: X- and Y- slices through the disk at Y- and X-coordinates of 240, 160, 80, 0 AU, respectively for the model KVZ0. Colour regions denote the equal projected velocity in the line-of-sight (S-axis).

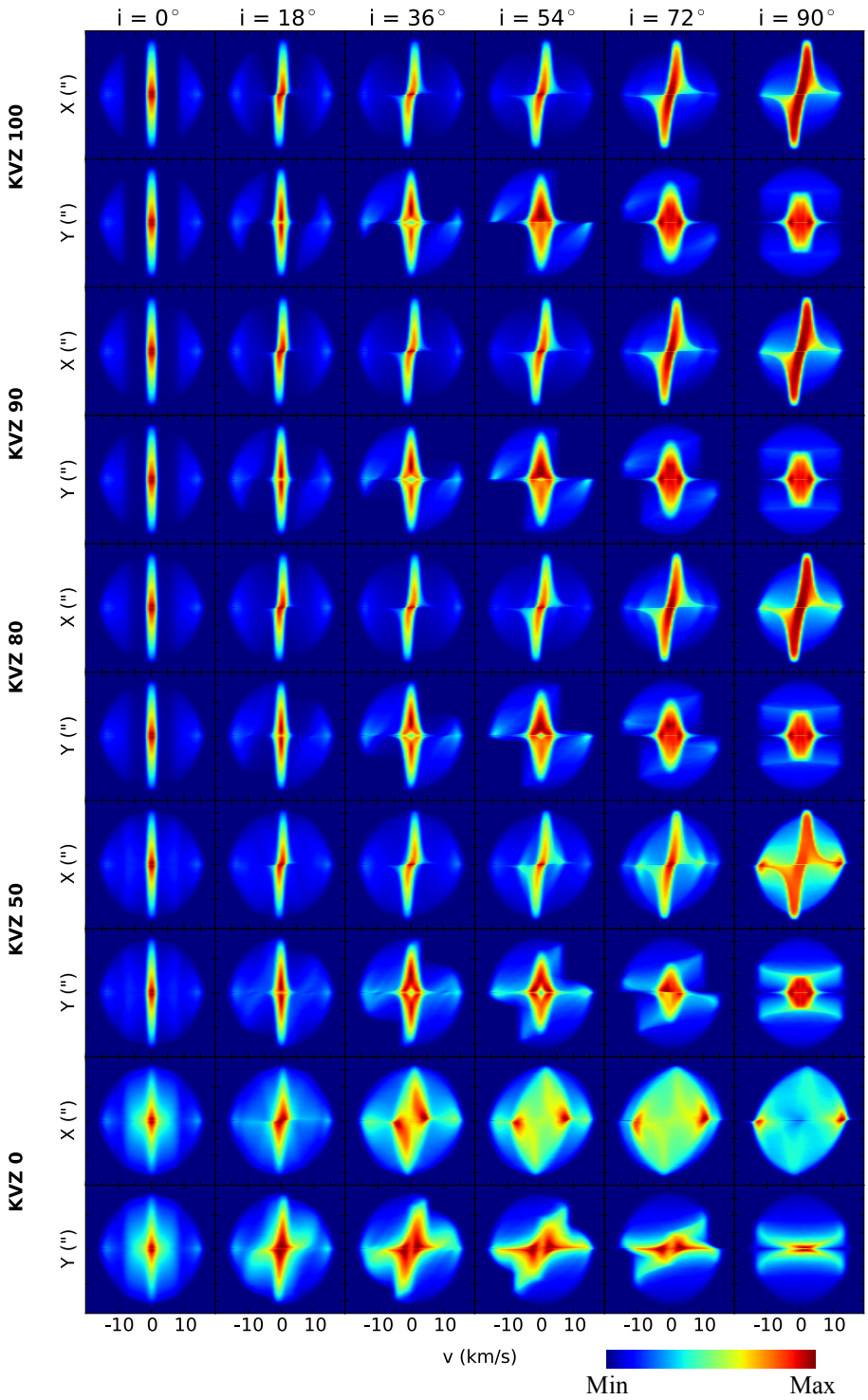

Figure 6.16: The PV-diagrams of the models KVZ100, KVZ90, KVZ80, KVZ50 and KVZ0, each spanned over two rows. The top row of each model represents a collapse of the 3D data cube onto the X-axis. The bottom row of each model represents the collapse of this data cube onto Y-axis. Each column presents an image of the PV-diagram at a different inclination angle. The colours represent the amount of flux with red the maximum amount and blue the least. It is important to note that none of the PV-diagrams are on the same scale. The bottom axis represents projected velocity space. Each model takes parameter values according to Tabel 5.2. This grid of models shows the impact of the Keplerian disk fraction on the PV-diagram.

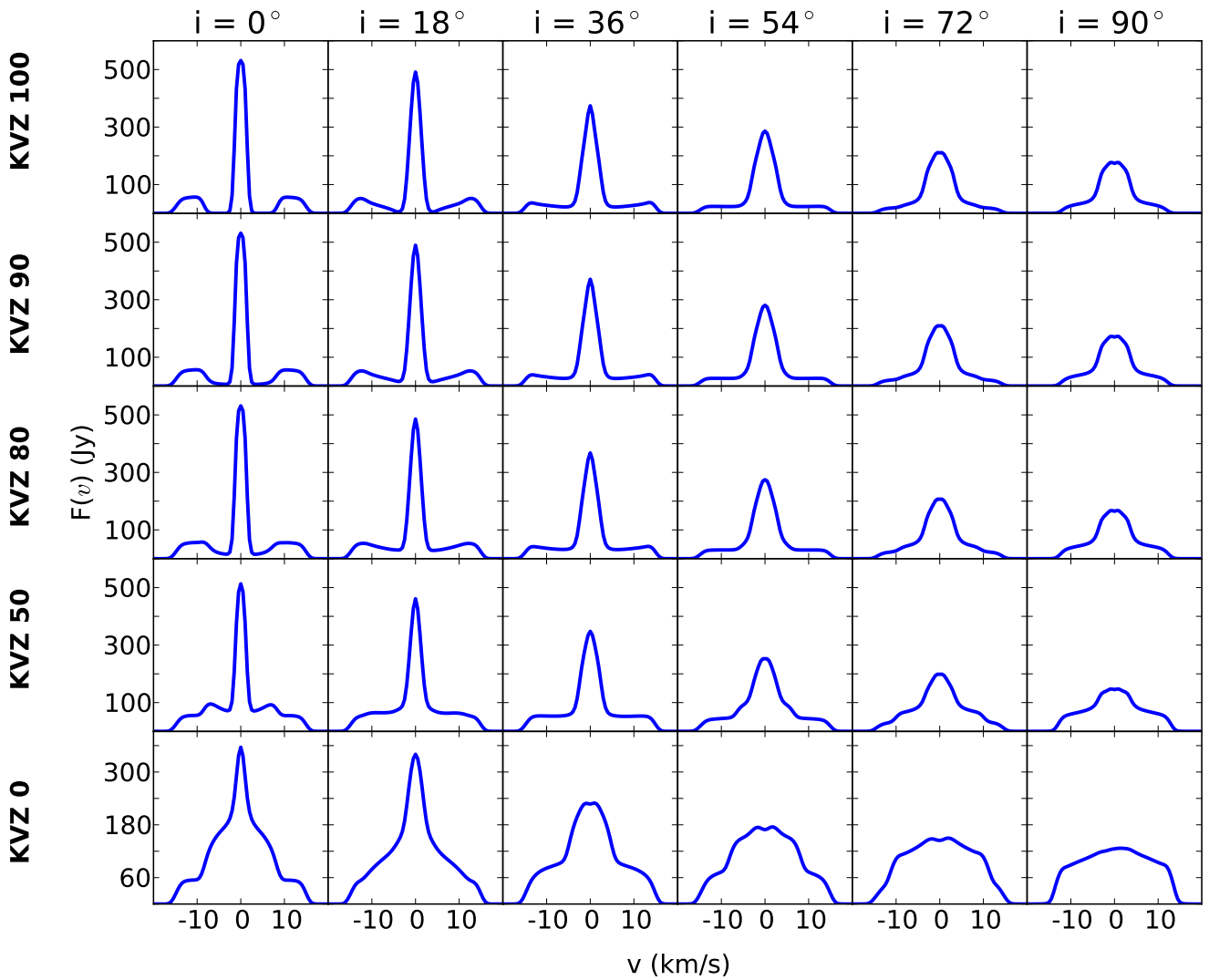

Figure 6.17: Line profiles for the models KVZ100, KVZ90, KVZ80, KVZ50 and KVZ0 with their parameter combination given in Tabel 5.2. Each column represents an inclination angle by which the structure is oriented. The line profiles denote the amount of flux in Jansky as a function of velocity in the line-of-sight.

6.5 Non-observable properties

Up to this point, we discussed the significant impact of three model parameters. Yet, there are still numerous parameters which we kept fixed but in principal can be varied. When you think of temperature, density or velocity, you would assume that these physical quantities will have some influence on the global object and will therefore present itself in the output data. Nevertheless, we have ascertained that this is not always true when inspecting the PV-plots or line profiles. Different density profiles, within the theoretical framework established above, do not significantly alter the PV-maps or line profiles. This is the case for the slightly different steepening temperature profiles. As this latter is theoretically coupled to the amount of flaring of the disk, via relation (4.55), the physical shape of the disk will not be extractable from PV-plot nor line profiles. Note that our simulated data is scale free but in real-life we observe absolute intensity which might act a a probe for the density and temperature profile. Modelling different CO rotational lines, which are temperature dependent, might also give more insight this these profiles due to their relative changes.
A fast accelerating wind is indistinguishable from a wind with constant velocity as this acceleration mainly occurs in the inner region and rapidly reaches its terminal velocity. Therefore it will be even less likely that we are able to differentiate between different accelerating wind profiles. It might be possible when we are dealing with a slowly accelerating wind. However, this completely misses the goal of the PV-diagrams and line profiles. They serve as a tool to be able to infer and compare morphological features for a wide range of object possibilities.

CHAPTER 7

Conclusion

Coming back to the main goal of this thesis: "Providing an overview of observable features intrinsic to certain morphologies of the structure within the outflows of evolved stars.", where we limited ourselves to a disk-like structure with a bipolar outflow. We aspired to achieve this goal by solving the inverse problem of deriving a three dimensional velocity distribution from two dimensional images. The fact that we are only able to observe velocity components projected into our line-of-sight and we have no idea how our object is oriented, makes this even more challenging. This thesis research has succeeded in performing the first steps towards the ultimate goal of being able to model complex morphologies in these outflows. We started from a simple analytic model for which we simulated observable data. Furthermore, this output has been manipulated into position-velocity diagrams and line profiles in order to be usable not only to infer different parameter impacts but as well for comparison with realistic observations. The former is performed for three different parameters, namely the rate of mass loss of the central star, the mass of the circumstellar disk and the fraction of the disk which rotates with a Keplerian velocity law. Since the orientation of the object plays a crucial role for observations, the impact of inclination is considered as well. An extended overview of these parameter impacts on the position-velocity diagrams and line profiles is presented in Chapter 6.

The disk and wind morphologies give rise to quite distinct shapes in the position-velocity diagrams. This enables us to purposely search for this peculiarities in observed data. As both disk and bipolar wind show largely different shapes, we are able to disentangle them and infer some of their

properties. Taking a quick glance at the line profile can already infers a lot of information because we know how wind and disk contribute to this line. As expected, the inclination has a tremendous effect on both position-velocity maps and line profiles. This allows the observer to constrain the inclination which will facilitate the determination of other properties. Line profiles and position-velocity diagrams are complementary tools to more efficiently disentangle wind from disk therefore creating a more correct view of the three dimensional kinematics and morphology of the object.

Within this thesis framework, we did not only provide the building blocks of a much larger goal, we have also demonstrated that it is possible to determine kinematic and morphological properties of such an object. Both position-velocity maps and line profiles enable the observer to determine the ratio of mass loss rate and disk mass. Our introduction of a transition zone which smooths out wind-disk interactions at their boundary, allows us to make an estimate of the velocity field in this region of real astronomical objects.
But not all properties are derivable from these manipulated tools. Temperature nor density profiles within such a disk can be inferred from them. Both contribute similar to the output as an increase in temperature or density results in an increase in yielded intensity, hence these parameters are degenerate. However, absolute intensity maps of real observations might allow us to probe these distributions. The relative differences between different CO rotational lines, which are a measure for temperature, may act as a probe as well. We limited ourselves to simple analytic profiles as at present time we do not have a good theoretically substantiated temperature nor density profiles. We did not probe more complex distributions because without a theoretical basis it is not useful to randomly start guessing. Theory suggests that disks will exhibit flared edge. We however determined that the amount of flaring will not be visible in the position-velocity diagrams and even less so in the line profiles. As an accelerating wind rapidly reaches its terminal velocity, it becomes indistinguishable from our constant velocity wind. Hence, it will not be possible to differentiate between different accelerating winds from PV-plots or line profiles for real astronomical observations.

Chapter 8

Future prospects

This thesis research represents the foundation for disk morphology studies in outflows of evolved stars. Therefore, several improvements can be made. Continuing on this particular model, a better criterion for the distinction between disk and wind can be sought after. Our geometric separation is still justified by a loss of only 5% of disk mass but a non-geometric separation based on physical quantities will surely be more realistic. Subsequently, the velocity profile in our transition zone is very crude. A velocity profile which considers the physical impacts of two mediums of different density shearing with different velocities, will better describe reality. It is most likely that Kelvin-Helmholtz instabilities will arise. Taking into account the correlation between properties of disk and wind, and the shearing impacts will provide a transition zone which leans more closely to reality. As stated before, simulating other CO rotational lines might allow us to probe the temperature distribution within our object.

The next step in the process is to simulate instrumental artefacts onto our output. For this the Common Astronomy Software Applications (CASA, McMullin et al., 2007) package can be used. This will allow us to state which observables are visible from actual observations. It is also a tool to figure out which dish, antenna and baseline settings of *ALMA* are most suitable for our disk-like object. These correctly simulated observational data can then be compared with actual observations. Performing this latter for a multitude of disk objects will provide insight in the physical properties and enable us to revise our theoretical understanding of disks in evolved stars. Our simple analytic model can then extended according to this more complete theory.

This iterative process will keep increasing our knowledge of disks in AGB stars.

As the still limited amount of observations already reveal a wide range in velocity distributions, it will be useful to simulate these as well and not restrict ourselves to a simple Keplerian disk. According to observations, a symmetrically expanding disk and fast bipolar jets are two interesting velocity distributions. Combinations of suggested profiles will of course also be interesting to analyse. Consideration of magnetic fields by MHD simulation will also have an impact on the observational data.

A more correct temperature profile can be attained by iteratively solving radiative transfer of a disk which is also subjected to conservation of energy and thermal equilibrium, e.g. MCMax (Min et al., 2009). This output temperature profile can then be used as an input for `LIME` which makes our model more correct and will maybe allow for an analyse of its impact on the position-velocity diagrams and line profiles. As emission is very temperature dependent, a non-trivial distribution might give some unexpected results. Adopting output from hydrodynamical simulations as input in `LIME` will surely increase matching reality. In the far future, coupling with extended complex chemical networks will be necessary to fully comprehend these intricate objects.

The outflows of evolved stars still hold numerous secrets which we have not yet unveiled. Improvements in instrumentation and modelling capabilities will gradually reveal these mysteries. The complexities concealed within the dusty envelopes of AGB stars are far from understood. This thesis has laid the foundation to shed light on this so far unresolved conundrum.

Bibliography

Alcolea, J., Neri, R., & Bujarrabal, V. 2007, A&A, 468, L41

Andrews, S. M., & Williams, J. P. 2007, ApJ, 659, 705

Andrews, S. M., Wilner, D. J., Hughes, A. M., Qi, C., & Dullemond, C. P. 2009, ApJ, 700, 1502

—. 2010, ApJ, 723, 1241

Balick, B., & Frank, A. 2002, ARA&A, 40, 439

Balick, B., Huarte-Espinosa, M., Frank, A., et al. 2013, ApJ, 772, 20

Bedding, T. R., & Zijlstra, A. A. 1998, ApJ, 506, L47

Bowen, G. H. 1988, in Astrophysics and Space Science Library, Vol. 148, Pulsation and Mass Loss in Stars, ed. R. Stalio & L. A. Willson, 3

Bowers, P. F., & Johnston, K. J. 1990, ApJ, 354, 676

Brinch, C., & Hogerheijde, M. R. 2010, A&A, 523, A25

Bujarrabal, V., & Alcolea, J. 2013, A&A, 552, A116

Bujarrabal, V., Alcolea, J., Van Winckel, H., Santander-García, M., & Castro-Carrizo, A. 2013, A&A, 557, A104

Bujarrabal, V., Castro-Carrizo, A., Alcolea, J., & Neri, R. 2005, A&A, 441, 1031

Bujarrabal, V., Castro-Carrizo, A., Alcolea, J., & Van Winckel, H. 2015, A&A, 575, L7

Bujarrabal, V., Fuente, A., & Omont, A. 1994, VizieR Online Data Catalog, 328, 50247

Castro-Carrizo, A., Neri, R., Bujarrabal, V., et al. 2012, A&A, 545, A1

Charbonnel, C. 1994, A&A, 282, 811

Chiang, E. I., & Goldreich, P. 1997, ApJ, 490, 368

Chiu, P.-J., Hoang, C.-T., Dinh-V-Trung, et al. 2006, ApJ, 645, 605

Cox, A. N. 2000, Allen's astrophysical quantities

Cox, N. L. J., Kerschbaum, F., van Marle, A.-J., et al. 2012, A&A, 537, A35

Davis, S. S. 2005, ApJ, 627, L153

De Beck, E., Decin, L., de Koter, A., et al. 2010, A&A, 523, A18

Debye, P. 1909, Annalen der Physik, 335, 57âĂŞ136

Decin, L., Cox, N. L. J., Royer, P., et al. 2012, A&A, 548, A113

García-Segura, G., Villaver, E., Langer, N., Yoon, S.-C., & Manchado, A. 2014, ApJ, 783, 74

Groenewegen, M. A. T., Barlow, M. J., Blommaert, J. A. D. L., et al. 2012, A&A, 543, L8

Hanner, M. S. 1988, Infrared Observations of Comets Halley and Wilson and Properties of the Grains, Tech. rep.

Hartmann, L., Calvet, N., Gullbring, E., & D'Alessio, P. 1998, ApJ, 495, 385

Hayashi, C. 1981, Progress of Theoretical Physics Supplement, 70, 35

Hirano, N., Shinnaga, H., Dinh-V-Trung, et al. 2004, ApJ, 616, L43

Homan, W., Decin, L., de Koter, A., et al. 2015, ArXiv e-prints, arXiv:1504.04996

Huggins, P. J. 2007, ApJ, 663, 342

Jeffers, S. V., Min, M., Waters, L. B. F. M., et al. 2014, A&A, 572, A3

Kahane, C., Cernicharo, J., Gomez-Gonzalez, J., & Guelin, M. 1992, A&A, 256, 235

Kahane, C., Dufour, E., Busso, M., et al. 2000, A&A, 357, 669

Kenyon, S. J., & Hartmann, L. 1987, ApJ, 323, 714

Kervella, P., Montargès, M., Ridgway, S. T., et al. 2014, A&A, 564, A88

Kim, H., Hsieh, I.-T., Liu, S.-Y., & Taam, R. E. 2013, ApJ, 776, 86

Kitamura, Y., Momose, M., Yokogawa, S., et al. 2002, ApJ, 581, 357

Kraemer, K. E., Hora, J. L., Egan, M. P., et al. 2010, AJ, 139, 2319

Lay, O. P., Carlstrom, J. E., & Hills, R. E. 1997, ApJ, 489, 917

Lykou, F., Klotz, D., Paladini, C., et al. 2015, A&A, 576, A46

Lynden-Bell, D., & Pringle, J. E. 1974, MNRAS, 168, 603

Maercker, M., Ramstedt, S., Leal-Ferreira, M. L., Olofsson, G., & Floren, H. G. 2014, A&A, 570, A101

Maercker, M., Mohamed, S., Vlemmings, W. H. T., et al. 2012, Nature, 490, 232

Malek, S. E., & Cami, J. 2014, ApJ, 794, 113

Mauron, N., & Huggins, P. J. 2000, A&A, 359, 707

McMullin, J. P., Waters, B., Schiebel, D., Young, W., & Golap, K. 2007, in Astronomical Society of the Pacific Conference Series, Vol. 376, Astronomical Data Analysis Software and Systems XVI, ed. R. A. Shaw, F. Hill, & D. J. Bell, 127

Men'shchikov, A. B., Balega, Y., Blöcker, T., Osterbart, R., & Weigelt, G. 2001, A&A, 368, 497

Mie, G. 1908, Annalen der Physik, 330, 377

Min, M., Dullemond, C. P., Dominik, C., de Koter, A., & Hovenier, J. W. 2009, A&A, 497, 155

Mundy, L. G., Looney, L. W., Erickson, W., et al. 1996, ApJ, 464, L169

Olivier, E. A., Whitelock, P., & Marang, F. 2001, MNRAS, 326, 490

Pérez-Sánchez, A. F., Vlemmings, W. H. T., Tafoya, D., & Chapman, J. M. 2013, MNRAS, 436, L79

Ramstedt, S., Schöier, F. L., Olofsson, H., & Lundgren, A. A. 2008, A&A, 487, 645

Ramstedt, S., Mohamed, S., Vlemmings, W. H. T., et al. 2014, A&A, 570, L14

Ritzerveld, J., & Icke, V. 2006, Phys. Rev. E, 74, 026704

Schöier, F. L., Maercker, M., Justtanont, K., et al. 2011, A&A, 530, A83

Schöier, F. L., & Olofsson, H. 2000, A&A, 359, 586

Schöier, F. L., van der Tak, F. F. S., van Dishoeck, E. F., & Black, J. H. 2005, A&A, 432, 369

Schwarzschild, M., & Härm, R. 1965, ApJ, 142, 855

Skinner, C. J., Meixner, M., & Bobrowsky, M. 1998, MNRAS, 300, L29

Soker, N. 1997, ApJS, 112, 487

Speck, A. K., Corman, A. B., Wakeman, K., Wheeler, C. H., & Thompson, G. 2009, ApJ, 691, 1202

Srinivasan, S., Sargent, B. A., Matsuura, M., et al. 2010, A&A, 524, A49

Teyssier, D., Hernandez, R., Bujarrabal, V., Yoshida, H., & Phillips, T. G. 2006, A&A, 450, 167

Toomre, A. 1964, ApJ, 139, 1217

Ueta, T. 2006, ApJ, 650, 228

van Marle, A. J., Cox, N. L. J., & Decin, L. 2014, A&A, 570, A131

van Winckel, H., Lloyd Evans, T., Briquet, M., et al. 2009, A&A, 505, 1221

Vassiliadis, E., & Wood, P. R. 1993, ApJ, 413, 641

Weidenschilling, S. J. 1977, Ap&SS, 51, 153

Weigert, A. 1966, Zeitschrift Astrophysics, 64, 395

Wilner, D. J., Ho, P. T. P., Kastner, J. H., & Rodríguez, L. F. 2000, ApJ, 534, L101

DEPARTMENT OF PHYSICS and ASTRONOMY
Celestijnenlaan 200d - box 2412
3001 HEVERLEE, BELGIË
tel. + 32 16 32 71 24
fys.kuleuven.be